Master's Thesis
Theoretical Physics

Optimal Quantum Driving for Single-Qubit Gates

Joni Ikonen
17.12.2015

Instructors: Prof. Mikko Möttönen
Dr. Juha Salmilehto
Supervisors: Prof. Mikko Möttönen
Prof. Kari Rummukainen

University of Helsinki
Department of Physics

PL 64 (Gustaf Hällströmin katu 2)
00014 Helsingin yliopisto

HELSINGIN YLIOPISTO — HELSINGFORS UNIVERSITET — UNIVERSITY OF HELSINKI

Tiedekunta/Osasto — Fakultet/Sektion — Faculty	Laitos — Institution — Department
Faculty of Science	Department of Physics

Tekijä — Författare — Author

Joni Ikonen

Työn nimi — Arbetets titel — Title

Optimal Quantum Driving for Single-Qubit Gates

Oppiaine — Läroämne — Subject

Theoretical Physics

Työn laji — Arbetets art — Level	Aika — Datum — Month and year	Sivumäärä — Sidoantal — Number of pages
Master's Thesis	12.2015	59

Tiivistelmä — Referat — Abstract

Quantum computers store and manipulate information in individual quantized energy levels. These devices, not yet realized in their full potential, have the ability to perform certain computational tasks more efficiently than any classical computer. One possible way to implement a quantum computer is to use superconducting circuits controlled by single-mode electromagnetic fields. These circuits constitute the physical quantum bits, or qubits, that are used to store quantum information. A complete, fault-tolerant quantum computer potentially consists of at least millions of physical qubits which are grouped to form fault-tolerant logical qubits. Controlling each physical qubit individually requires a great amount of energy, and hence a future challenge is to reduce the energy consumption in qubit control while maintaining the high precision.

In this thesis, we derive a fundamental upper bound for the gate fidelity of a single-qubit NOT gate implemented with a single resonant driving pulse. It is shown that the upper bound approaches unity inversely proportionally to the increasing mean photon number of the pulse. Furthermore, we find that the upper bound is achieved with an optimal superposition of squeezed states. The typically employed coherent state produces twice as high gate error as the corresponding optimal state.

In addition, we present and numerically study a correction protocol that allows using the same drive state for multiple qubit operations. This sustained state is refreshed by sequentially coupling ancillary qubits to it, effectively resetting it and removing entanglement with the previously operated qubits. Thus our protocol allows using the same drive state to implement NOT gates for different qubits indefinitely, and hence provides a possible route to energy-efficient large-scale quantum computing.

Avainsanat — Nyckelord — Keywords

Jaynes–Cummings model, quantum driving, qubit, fidelity, NOT gate

Säilytyspaikka — Förvaringsställe — Where deposited

Muita tietoja — övriga uppgifter — Additional information

Preface

The work for this thesis was carried out in the Quantum Computing and Devices (QCD) group in the Department of Applied Physics of Aalto University. My profound thanks to Prof. Mikko Möttönen, the leader of the QCD group, who provided the opportunity to work on this topic and guided me through the process with his infinite supply of insightful suggestions. I also thank Dr. Juha Salmilehto for his valuable feedback and verification of calculations.

I would like to thank Prof. Kari Rummukainen for formally supervising this thesis at the University of Helsinki and especially acknowledge Dr. Paolo Solinas for his encouraging comments and useful discussion. For companionship and interesting discussions I would like to thank B.Sc. Santeri Kaupinmäki, M.Sc. Máté Jenei, and everyone else in the QCD group. Finally, I express my gratitude to my family and friends, who supported me all this time.

Espoo, December 2015

Joni Ikonen

Contents

1 Introduction

Quantum computers [1, 2] are one of the most intriguing practical applications of quantum mechanics. The power of quantum computers is based on the principle of superposition, a property that emerges only in coherent quantum systems. Similar to electrical bits of an ordinary computer, a quantum computer stores its information in quantum-mechanical two-level systems, known as quantum bits, or qubits. The crucial advantage is that the value of a qubit is not restricted to either 0 or 1, but may be in a superposition of the two. In principle, this simple yet unintuitive property, along with the ability to prepare, manipulate, and read the qubit information, allows constructing computational algorithms more powerful than any classical algorithm [1]. These algorithms can be used in tasks that cannot otherwise be executed efficiently, such as factoring large numbers, searching large unordered data sets, and simulating quantum mechanical systems [2]. This was demonstrated in the 1990's with the Deutsch–Jozsa [3], Shor's [4], and Grover's [5] algorithms, for example. Today, the major challenge is to develop technology that is able to execute quantum algorithms with minimal error.

To serve as a useful platform for quantum computation, a system needs to fulfill a number of requirements, first listed by DiVincenzo [6]. The obvious requirement is that the system exhibits distinct quantum properties, such as the coherent superposition of qubit states. In addition, the qubits must provide high-precision in their preparation, control, and measurement while simultaneously being resistant to environmental noise. This imposes challenges: a qubit that is strongly coupled to the driving system usually also couples strongly to the decoherence-inducing environment. On the other hand, weakly coupled systems are typically more difficult to entangle and control [1]. Much of the current research is centered around finding a way to achieve both precise control and resistance to decoherence.

Many different technologies have been suggested as a platform for quantum computers. The earliest schemes envisioned atoms flying through cavities filled with microwave radiation [7]. The information would be carried by the atom states, while the cavities would act as gates, i.e., elements of the computer that perform chosen operations. The modern modification of this method uses ions that are optically trapped and controlled with lasers [8]. A completely different approach is to use photons as the information carriers. In this case, the qubit information is encoded in, for example, different polarizations of light and the gates are constructed with beam splitters and wave plates [9]. Other possible realizations for qubits include nuclear spins controlled by resonant magnetic fields [10], and electron spins in quantum dots or donor atom potentials [11].

The most advanced quantum computer to date [12] is based on solid-state supercon-

ductors at sub-kelvin temperatures. The most appealing features of this technology, known as circuit quantum electrodynamics (cQED), are precise qubit control and straightforward scaling possibilities [2]. The state-of-the-art superconducting qubits, known as transmons or Xmons [12], essentially consist of an LC-circuit where Cooper pairs travel across a Josephson junction and have a collective energy spectrum similar to that of an anharmonic oscillator [13]. Due to the nonlinear inductance of the Josephson junction, the spectrum can be utilized as an effective two-level system. Despite its macroscopic size, this construction has the required properties of a qubit [13]. The state of the qubit is controlled by microwave pulses which are capacitively coupled to the circuit, either directly or through a microwave resonator. The cQED systems and many other driven qubits are modeled with the Jaynes–Cummings model, describing the dynamics of a two-level system coupled to a bosonic field [14].

Each of the technologies has disadvantages. A few trapped ions can be controlled with high precision, but increasing the amount of qubits while keeping the same level of precision is challenging [8]. In the case of photon qubits, the greatest obstacle is to reliably transfer information between the photons [2], whereas the nuclear spin qubits are difficult to initialize [1]. The early implementations of the superconducting qubits were susceptible to noise and decoherence, while the electron spin qubits were challenging to couple. However, as demonstrated by recent experiments [15, 16], the possible error sources in solid-state cQED have been reduced enough to allow fault-tolerant computation with error correction.

The inevitable errors can be accounted for by implementing a quantum error correction code [17]. This is possible by coding the information of one logical qubit into a large ensemble of physical qubits. Even without accessing the information content of the logical qubit, a proper error correction code can measure and correct the possible errors in the physical qubits [17]. One of the most tolerant type of correction codes are surface codes which allow reliable computation if the single-step error is below a modest threshold of 1% [18]. Recently, single-qubit gates with 0.08% gate error have been demonstrated using superconducting circuits [15], along with precise measurement and two-qubit control. These result in a single-step error which is well below the tolerance threshold of the surface code, implying a significant step towards robust, large-scale quantum computers. The drawback of the surface code is that a fault-tolerant logical qubit requires an order of 10^3–10^4 physical qubits [18]. However, the number of physical qubits can be decreased significantly by increasing the precision of the qubit operations. Alternative error correction codes [19] require less physical qubits per logical qubit at the expense of more stringent thresholds.

Since large-scale quantum computers seem to emerge in the near future, it is important to consider the trade-off between energy consumption and precision in qubit control. In cQED,

each single-qubit operation is realized with a microwave pulse which decoheres and entangles with the qubit due to the quantum back-action and therefore should not be used repeatedly as such. The amount of energy required per pulse may be small, but cannot be neglected if the number of physical qubits is 10^5 or more. The question of energy consumption is enforced even more by the fact that this computer must operate at temperatures below 100 mK, making cooling and efficient heat conduction challenging. This raises the need to decrease the dissipated power per qubit while improving their operation fidelity.

Thus we arrive at the following research questions: with a given pulse energy, is there a limit on the best achievable fidelity? With what kind of pulse is this limit achieved? Is the coherent pulse, commonly used in qubit operations, the optimal one? Is it possible to remove the entanglement between the qubits and the drive, so that a single drive pulse could be used for many operations, perhaps even indefinitely? This thesis answers these questions. The first four chapters provide an introduction to the mathematics and physics of cQED. The main results of the thesis are derived and discussed in Chapters 5–9.

In Chapter 2, we present the mathematical framework and formalism needed in the subsequent chapters. This includes brief introductions to density operators, quantum operations applied to qubits, and quantized bosonic fields. Some useful concepts, such as fidelity, the Bloch sphere, and the Wigner function are also discussed. Chapter 3 briefly presents the dynamics of superconducting circuits in a scope needed for this thesis. In Chapter 4, we use these tools to study the coupling of qubits and photons. We solve the dynamics of an ideal Jaynes–Cummings system and note some of its most important features, such as Rabi oscillations.

In Chapters 5 and 6, the main results of this thesis are presented. We write an expression for the fidelity of a bit flip state transformation, with a given interaction time, and extremize it with respect to all possible drive states. This eventually provides an expression for the upper bound for gate fidelity, along with the corresponding optimal drive state. We also show that the optimal states produce smaller errors than the corresponding coherent states. We find that the optimal pulses can be produced experimentally with known techniques, allowing the energetically optimal NOT gate to be implemented in practice.

In Chapter 8, we take this research a step further, and present a procedure where a single drive state can be used multiple times for sequential gates. Namely, the drive state can be restored to its initial value by sequentially coupling auxiliary qubits to it, thus erasing the inevitable decoherence and entanglement caused by the quantum back-action. This way, in principle, an infinite amount of operations can be performed without creating a new pulse for each operation. Finally, our results are summarized in Chapter 9.

2 Mathematical preliminaries

In this chapter, we introduce the concepts, tools, and notations used in the following chapters. The topics include the most common representations for qubits and electromagnetic fields, along with the mathematical tools of density operators, quantum gates, purity, fidelity, and ladder operators.

2.1 Quantum bits

According to the postulates of quantum mechanics, any physical system can be described completely by a Hilbert space and operators acting on it [1]. The state of the system is represented by the state vector, which is an element of this space. The two Hilbert spaces used in this thesis are the two-dimensional space $\mathcal{H}_{\mathrm{Q}}$ and the infinite-dimensional Fock space $\mathcal{H}_{\mathrm{D}}$, which represent a two-level system and a bosonic electromagnetic mode, respectively.

Quantum bits, commonly known as qubits, are here the elementary units of information. They are counterparts of bits in a classical computer. Any physical system that is effectively described by a two-dimensional Hilbert space $\mathcal{H}_{\mathrm{Q}}$ is a potential candidate for a qubit [18].

In this thesis, we only consider qubits that have non-degenerate energy levels. Thus for the two-dimensional space, we choose a basis spanned by the energy eigenstates $|\mathrm{g}\rangle$ and $|\mathrm{e}\rangle$. The labels refer to the ground and excited state, respectively. In quantum computing, the logical values 0 and 1 are assigned to these states. Any qubit state $|\chi\rangle$ may be expressed as

$$|\chi\rangle = z\,|\mathrm{e}\rangle + w\,|\mathrm{g}\rangle\,, \tag{2.1}$$

where the amplitudes z and w are complex numbers restricted by the normalization condition $|z|^2 + |w|^2 = 1$. Using this condition and excluding a physically irrelevant common phase factor, $|\chi\rangle$ can equivalently be written as

$$|\chi\rangle = z\,|\mathrm{e}\rangle + \sqrt{1-|z|^2}\,|\mathrm{g}\rangle\,, \tag{2.2}$$

with $|z| \leq 1$. Thus the state of the qubit is completely determined by the complex *qubit value* z.

Where matrix representations are used, we follow the convention

$$|\mathrm{g}\rangle \mathrel{\widehat{=}} \begin{pmatrix} 1 \\ 0 \end{pmatrix}, \quad |\mathrm{e}\rangle \mathrel{\widehat{=}} \begin{pmatrix} 0 \\ 1 \end{pmatrix}. \tag{2.3}$$

In a general case, we represent qubits with density operators in this basis, as discussed in Sec. 2.3.

2.2 Fock space

To describe the electromagnetic mode that drives the qubits, an infinite-dimensional Hilbert space is needed. Employing the method of second quantization, the electromagnetic field can be expressed using the Fock space [20]. For simplicity, we assume that the field is described by a single mode of well-defined frequency. The most convenient formalism for such system consisting of identical bosons is the occupation number representation, in which the space is spanned by the *number states* $|n\rangle$, where $n \geq 0$ is the number of excitations, i.e., photons, in the field.

The number states are connected via *creation* and *annihilation operators* [20], also known as the ladder operators

$$\hat{a} = \sum_{m=0}^{\infty} \sqrt{m}\, |m-1\rangle\langle m| \,, \tag{2.4}$$

$$\hat{a}^\dagger = \sum_{m=0}^{\infty} \sqrt{m+1}\, |m+1\rangle\langle m| \,. \tag{2.5}$$

They obey the commutation relation $\left[\hat{a},\, \hat{a}^\dagger\right] = 1$, characteristic of all bosonic systems. The effect of these operators is to lower or raise the number of excitations by one. For example, we can construct a number state $|n\rangle$ using the vacuum state $|0\rangle$ and the creation operator

$$|n\rangle = \frac{1}{\sqrt{n!}} \left(\hat{a}^\dagger\right)^n |0\rangle \,. \tag{2.6}$$

Another important operator is the number operator $\hat{N} = \hat{a}^\dagger \hat{a}$, the eigenvalue of which is the photon number itself, $\hat{N}\,|n\rangle = n\,|n\rangle$.

2.2.1 Special states and operators

In addition to the number states, there are certain superpositions of Fock states that have special properties. The most commonly known example is the coherent state [20]

$$|\mathrm{D}_\alpha\rangle = \mathrm{e}^{-\frac{1}{2}|\alpha|^2} \sum_{n=0}^{\infty} \frac{\alpha^n}{\sqrt{n!}} |n\rangle \,, \tag{2.7}$$

where α is a complex number. The coherent state is an eigenstate of the annihilation operator, $\hat{a}\,|\mathrm{D}_\alpha\rangle = \alpha\,|\mathrm{D}_\alpha\rangle$. The probability of measuring n photons in a coherent state is $\mathcal{P}(n) = \mathrm{e}^{-|\alpha|^2}\,|\alpha|^{2n}/n!$, which is the Poisson distribution with the parameter $\lambda = |\alpha|^2$. The expectation value of the Poisson distribution is λ, and thus the average number of photons in a coherent state is given by $\overline{n} \equiv \langle\hat{N}\rangle = |\alpha|^2$. If $\overline{n} \gg 1$, the coherent state takes the form of a normal distribution, resembling a classical state with definite, macroscopic energy. For this reason, the coherent state is sometimes referred to as the classical state of light [20], as opposed to the non-classical number states.

Another way of expressing the coherent state is given by the *displacement operator*

$$\hat{\mathcal{D}}(\alpha) \;=\; \mathrm{e}^{\alpha\hat{a}^\dagger - \alpha^*\hat{a}}. \tag{2.8}$$

The effect of $\hat{\mathcal{D}}(\alpha)$ is to shift the probability distribution $\mathcal{P}(n)$ by $|\alpha|^2$. The coherent state can be produced by displacing the vacuum [21]

$$|\mathrm{D}_\alpha\rangle = \hat{\mathcal{D}}(\alpha)\,|0\rangle\,. \tag{2.9}$$

Another useful operator is the *squeezing operator* [21]

$$\hat{\mathcal{S}}(s) = \mathrm{e}^{\frac{1}{2}\left[s^*\hat{a}^2 - s\left(\hat{a}^\dagger\right)^2\right]}. \tag{2.10}$$

Operating on a coherent state, the effect of the squeezing is to reshape the probability distribution $\mathcal{P}(n)$ to sub-Poissonian or super-Poissonian, depending on the phase of the complex parameter s. Combining the two operators we obtain the so called squeezed states, $|\mathrm{S}_\alpha^{(\mathrm{s})}\rangle = \hat{\mathcal{D}}(\alpha)\hat{\mathcal{S}}(s)\,|0\rangle$, that have been observed experimentally [20]. The explicit expressions for the amplitudes of a squeezed state are quite complicated; for details see Ref. [21].

Assuming $s, \alpha \in \mathbb{R}$, the mean photon number and variance of $|\mathrm{S}_\alpha^{(\mathrm{s})}\rangle$ are given by [22]

$$\overline{n} \;=\; |\alpha|^2 + \sinh^2 s \tag{2.11}$$

$$\nu^2 \;=\; |\alpha|^2\,\mathrm{e}^{-2s} + 2\sinh^2 s\cosh^2 s. \tag{2.12}$$

If $|\alpha|^2$ is large compared to the other terms, the mean stays almost the same while the variance decreases ($s > 0$) or increases ($s < 0$). The coherent and squeezed states are illustrated in Fig. 2.1.

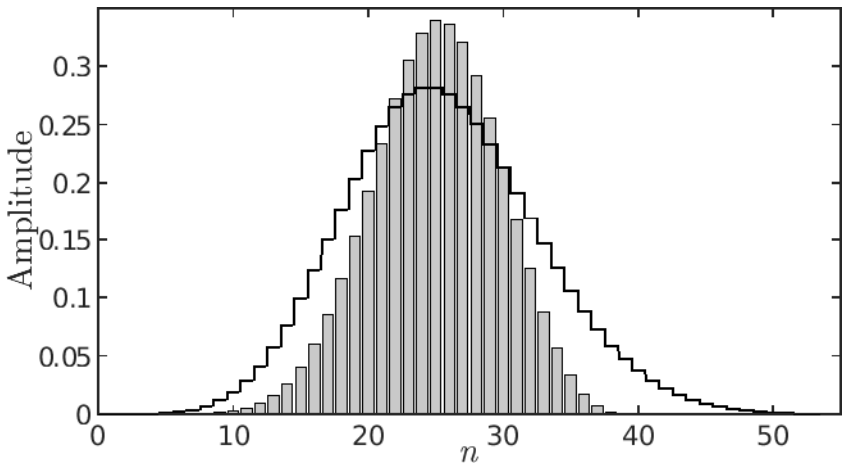

Figure 2.1: Amplitudes of a squeezed state (bars) and a coherent state (line). The displacement parameter of both states is $\alpha = 5$, resulting in an average photon number of $\langle \hat{N} \rangle = 5^2 = 25$. The squeezing parameter of the squeezed state is $s = 0.4$, making the distribution peak more strongly than the non-squeezed state.

2.3 Density operators

The temporal evolution of a closed system, described by the state $|\psi(t)\rangle$, is determined by the Hamiltonian operator $\hat{H}$ of the system, and the Schrödinger equation [23]

$$i\hbar \frac{\partial}{\partial t} |\psi(t)\rangle = \hat{H}(t) |\psi(t)\rangle \,, \tag{2.13}$$

where $\hbar$ denotes the reduced Planck constant. A formal solution is given by

$$|\psi(t)\rangle = \hat{\mathcal{T}} \mathrm{e}^{-i \int_0^t \hat{H}(t') dt'/\hbar} |\psi(0)\rangle \equiv \hat{U}(t) |\psi(0)\rangle \,, \tag{2.14}$$

where $\hat{\mathcal{T}}$ is the time-ordering operator that ensures the non-commuting Hamiltonians be sorted by increasing time. In the last equality, we have defined the *time evolution operator* $\hat{U}(t) = \hat{\mathcal{T}} \exp(-i \int_0^t \hat{H}(t') dt'/\hbar)$, which transforms the system from an initial state $|\psi(0)\rangle$ to a state at a later time t. The temporal evolution operator is a unitary operator.

When two quantum systems interact, say, the qubit and its environment, the separate systems are not closed and their evolution is not unitary in general. In a non-unitary evolution, the qubit state may decohere, an evolution that may be understood as a measurement by the environment [1]. In this case, the individual systems cannot be described by state vectors. Instead, the decoherent state can be represented by means of a *density operator*, a Hermitian operator of unit trace. The density operator is formulated as an ensemble of multiple state vectors, each with a corresponding probability. Formally, the density operator

$\hat{\rho}$ is defined as [1]

$$\hat{\rho} = \sum_i p_i \left|\psi_i\right\rangle\!\left\langle\psi_i\right| . \tag{2.15}$$

Here $|\psi_i\rangle$ are any state vectors of the Hilbert space, and the real positive coefficients p_i are classical probabilities for the respective states $|\psi_i\rangle$. Thus the coefficients must obey $\sum_i p_i = 1$. Given a complete orthonormal basis $\{|e_n\rangle\}$, the density operator can also be expressed in terms of a *density matrix* ρ_{nm} as

$$\begin{aligned} \hat{\rho} &= \sum_i p_i \left(\sum_n |e_n\rangle\langle e_n| \right) |\psi_i\rangle\langle\psi_i| \left(\sum_m |e_m\rangle\langle e_m| \right) \\ &= \sum_{nm} |e_n\rangle\langle e_m| \sum_i p_i \langle e_n \,|\, \psi_i\rangle\langle\psi_i \,|\, e_m\rangle \\ &\equiv \sum_{nm} |e_n\rangle\langle e_m| \, \rho_{nm}. \end{aligned} \tag{2.16}$$

A density operator with exactly one nonzero coefficient $p_i = 1$ corresponds to a *pure* state. The formalism of pure states reduces to that of state vectors. On the contrary, states with multiple nonzero coefficients $\{p_i\}$ are *mixed* [1]. A completely mixed state is represented by a diagonal density matrix, $\rho_{nm} = \delta_{nm} d^{-1}$, where d is the dimension of the Hilbert space and δ_{nm} is the Kroenecker delta. This ensemble has no quantum properties and all states have equal probability.

In the density operator formalism, the temporal evolution of a system is given by the von Neumann equation [23]

$$i\hbar \frac{\mathrm{d}}{\mathrm{d}t} \hat{\rho}(t) = \left[\hat{H}(t),\, \hat{\rho}(t) \right] . \tag{2.17}$$

which can be derived by multiplying the Schrödinger equation (2.13) with its Hermitian conjugate, and using Eq. (2.15). This guarantees that the dynamics of pure states reduces to those given by the Schrödinger equation. The solution of the von Neumann equation is formally $\hat{\rho}(t) = \hat{U}(t)\hat{\rho}(0)\hat{U}^\dagger(t)$, where the operator $\hat{U}(t)$ is defined in Eq. (2.14).

2.3.1 Partial trace

Often we are interested in the state of either the qubit or the field, rather than the system as a whole. The state of a desired component can be extracted from the larger state by taking the *partial trace* over the other component spaces. For an arbitrary density operator

$\hat{\rho} \in \mathcal{H}_\mathrm{A} \otimes \mathcal{H}_\mathrm{B}$, the partial trace over $\mathcal{H}_\mathrm{B}$ is defined as [1]

$$\mathrm{Tr}_\mathrm{B}\left(\hat{\rho}\right) = \sum_{n=1}^{d_\mathrm{B}} \mathrm{Tr}\left(\hat{\rho}\,\hat{\mathbb{I}}_\mathrm{A} \otimes |e_n\rangle\langle e_n|\right) \in \mathcal{H}_\mathrm{A}. \tag{2.18}$$

Here, $\hat{\mathbb{I}}_\mathrm{A}$ is the identity operator of $\mathcal{H}_\mathrm{A}$ and $\{|e_n\rangle\}$ are the basis states of $\mathcal{H}_\mathrm{B}$.

2.3.2 Purity

It is not immediately obvious whether an arbitrary density operator represented as a matrix in some basis is pure or mixed. An adequate indicator of the nature of the state is the trace $\mathrm{Tr}\left(\hat{\rho}^2\right)$. In the domain of possible density operators, it assumes values in the range $[1/d, 1]$. For this reason, we define the *purity* P of a state as [24]

$$P(\hat{\rho}) = \frac{d\,\mathrm{Tr}\left(\hat{\rho}^2\right) - 1}{d-1}, \tag{2.19}$$

where the rescaling has been introduced to have $P(\hat{\rho}) \in [0, 1]$. For pure states, the purity is 1 by definition since $\mathrm{Tr}\left(\hat{\rho}^2\right) = \mathrm{Tr}\left(|\psi\rangle\langle\psi\,|\,\psi\rangle\langle\psi|\right) = \mathrm{Tr}\left(\hat{\rho}\right) = 1$. On the other hand, $P = 0$ corresponds to a completely mixed state with $\rho_{nm} = \delta_{nm} d^{-1}$. The purity is also related to so-called linear entropy S by $P = 1 - S$, so a pure state is a state of minimal linear entropy, whereas a completely mixed state is has maximum linear entropy [24]. Thus this definition of purity serves as an intuitive measure of the quality of the state.

2.3.3 Fidelity

Another useful quantity is the *fidelity* F, which measures the overlap of two states. It is defined as[1]

$$F(\hat{\rho}_\mathrm{A}, \hat{\rho}_\mathrm{B}) = \mathrm{Tr}\left(\hat{\rho}_\mathrm{A}\hat{\rho}_\mathrm{B}\right). \tag{2.20}$$

Like purity, the fidelity is a monotonic function ranging from 0 (corresponding to orthogonal states) to 1 (equal states). For pure states, the fidelity simply reduces to the usual overlap of two state vectors, $F = |\langle\psi_\mathrm{A}\,|\,\psi_\mathrm{B}\rangle|^2$.

[1] Sometimes the fidelity is defined as $F(\hat{\rho}_\mathrm{A}, \hat{\rho}_\mathrm{B}) = \mathrm{Tr}\sqrt{\hat{\rho}_\mathrm{A}^{1/2}\hat{\rho}_\mathrm{B}\hat{\rho}_\mathrm{A}^{1/2}}$ [1]. The motivation behind this definition is that it coincides with the classical notion of fidelity. Compared to our definition, it only produces slightly different values in the range $]0, 1[$ but is a lot more cumbersome in practical calculations. Removing the square root reduces it to the definition of Eq. (2.20), used e.g. in Refs [15, 24, 25].

2.3.4 Bloch representation

An intuitive description of a qubit is offered by the Bloch representation, which maps a density operator to a three-dimensional vector. Any two-dimensional density matrix can be expressed using the Pauli spin matrices

$$\sigma_{\mathrm{x}} = \begin{pmatrix} 0 & 1 \\ 1 & 0 \end{pmatrix}, \quad \sigma_{\mathrm{y}} = \begin{pmatrix} 0 & -i \\ i & 0 \end{pmatrix}, \quad \sigma_z = \begin{pmatrix} 1 & 0 \\ 0 & -1 \end{pmatrix}, \tag{2.21}$$

as [26]

$$\rho = \begin{pmatrix} \rho_{\mathrm{gg}} & \rho_{\mathrm{ge}} \\ \rho^*_{\mathrm{ge}} & \rho_{\mathrm{ee}} \end{pmatrix} = \frac{1}{2}\left(\mathbb{I} + B_{\mathrm{x}}\sigma_{\mathrm{x}} + B_{\mathrm{y}}\sigma_{\mathrm{y}} + B_{\mathrm{z}}\sigma_z\right), \tag{2.22}$$

where $\mathbb{I}$ is the identity matrix and $\{B_i\}$ are the components of the *Bloch vector* $\mathbf{B}$. Explicit expressions for the components can be obtained by multiplying Eq. (2.22) by a corresponding Pauli matrix and taking a trace. They are given by

$$B_{\mathrm{x}} = 2\mathrm{Re}\left(\rho_{\mathrm{ge}}\right), \quad B_{\mathrm{y}} = -2\mathrm{Im}\left(\rho_{\mathrm{ge}}\right), \quad B_{\mathrm{z}} = \rho_{\mathrm{gg}} - \rho_{\mathrm{ee}}. \tag{2.23}$$

A Bloch vector of a pure state is confined to the surface of a unit sphere, whereas mixed states are mapped to inside the sphere. This restriction can be observed by inserting Eq. (2.22) into the definition of purity, whence

$$P(\hat{\rho}) = 2\,\mathrm{Tr}\rho^2 - 1 = |\mathbf{B}|^2 . \tag{2.24}$$

Thus the magnitude of the Bloch vector represents the purity of the state and $|\mathbf{B}|^2 \in [0, 1]$. The ground and excited states are mapped to the north and south pole of the sphere, respectively. The completely mixed state corresponds to the null vector.

In addition, the Bloch vector gives a visual representation of fidelity. Consider two pure qubits with Bloch vectors $\mathbf{B}_{\mathrm{A}}$ and $\mathbf{B}_{\mathrm{B}}$ ($|\mathbf{B}_{\mathrm{A}}| = |\mathbf{B}_{\mathrm{B}}| = 1$). Using Eqs. (2.20) and (2.22) we obtain

$$F(\hat{\rho}_{\mathrm{A}}, \hat{\rho}_{\mathrm{B}}) = \frac{1}{2}\left(1 + \mathbf{B}_{\mathrm{A}} \cdot \mathbf{B}_{\mathrm{B}}\right) = \cos^2\left(\frac{\theta_{\mathrm{AB}}}{2}\right), \tag{2.25}$$

where θ_{AB} is the angle between the two vectors. The higher the fidelity, the closer the Bloch vectors are to each other on the Bloch sphere.

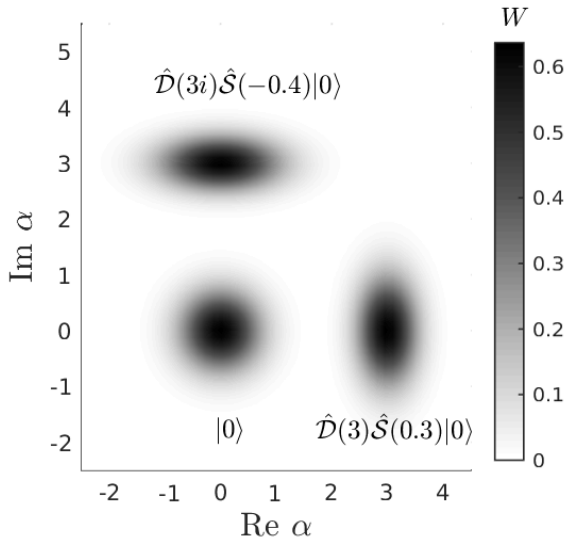

Figure 2.2: Action of the displacement and squeezing operators in the Wigner representation. The vacuum state yields a circular distribution centered at the origin. The rightmost distribution is obtained by squeezing the vacuum with a squeezing parameter $s = 0.3$ and then displacing the result with $\alpha = 3$. The topmost distribution is similarly obtained with the parameters $s = -0.4$ and $\alpha = 3i$.

2.3.5 Wigner pseudo-probability function

Density operators of the Fock space can be visualized with the Wigner pseudo-probability function. The Wigner function represents a density operator $\hat{\rho}$ in the complex plane, with the value at point z given by [27]

$$W(z) = \frac{2}{\pi}\mathrm{Tr}\left[\hat{\mathcal{D}}(-z)\hat{\rho}\hat{\mathcal{D}}(z)\mathrm{e}^{i\pi\hat{a}^\dagger\hat{a}}\right]. \tag{2.26}$$

The Wigner function represents the coherent states as Gaussian-like distributions, the peak center given by the displacement parameter α. In this space, the effect of the displacement and the squeezing operators are rather intuitive: $\hat{\mathcal{D}}(\alpha)$ shifts the location of the distribution by α, whereas $\hat{\mathcal{S}}(s)$ deforms the shape from circular to elliptical. The complex phase of the parameter s dictates the angle of the ellipse; with real s, the distribution is squeezed in the direction of the real axis and stretched along the imaginary axis. These effects are illustrated in Fig. 2.2.

2.4 Quantum gates

To manipulate the information stored in the qubits, we need to be able to change their states. Whereas the true evolution of the system is described by a specific Hamiltonian

operator, the abstract theory of quantum information is not tied to any particular physical system. Instead of specific operators corresponding to physical observables, the evolution of the qubits is typically studied with the help of ideal *quantum gates*. A quantum gate performs a certain logical operation typically on one or two qubits at a time.

A trace-preserving single-qubit gate $\hat{\Phi}$ acting on a density operator $\hat{\rho}$ can be expressed in the operator-sum form as [1]

$$\hat{\Phi}(\hat{\rho}) = \sum_i \hat{K}_i \hat{\rho} \hat{K}_i^\dagger, \tag{2.27}$$

where the so-called Kraus operators $\{\hat{K}_i\}$ must sum up to the identity operator, $\sum_i \hat{K}_i \hat{K}_i^\dagger = \hat{\mathbb{I}}$. For example, the quantum counterpart of the classical NOT operation $0 \leftrightarrow 1$, the quantum bit flip operation, is performed by the gate

$$\hat{\Phi}_{\mathrm{NOT}}(\hat{\rho}) \;=\; \hat{\sigma}_{\mathrm{x}} \hat{\rho} \hat{\sigma}_{\mathrm{x}}. \tag{2.28}$$

The quantum NOT gate corresponds to interchanging the basis vectors, $|\mathrm{g}\rangle \leftrightarrow |\mathrm{e}\rangle$.

Other useful gates include the phase flip and bit–phase flip gates, which correspond to the Pauli matrices $\hat{\sigma}_{\mathrm{z}}$ and $\hat{\sigma}_{\mathrm{y}}$, respectively. The effects of different quantum gates are conveniently visualized with the Bloch sphere. The X, Y, and Z gates rotate the Bloch vector of a state about the respective axes by π and are thus referred to as π rotations. Furthermore, rotations by $\pi/2$ are represented by $\sqrt{\hat{\sigma}_{\hat{\mathbf{n}}}}$, depending on the desired axis $\hat{\mathbf{n}}$. Up to a global phase shift, many other gates can be expressed by a combination of these operators, such as the Hadamard gate

$$\hat{\sigma}_{\mathrm{H}} = \hat{\sigma}_{\mathrm{x}} \sqrt{\hat{\sigma}_{\mathrm{y}}} \mathrel{\widehat{=}} \frac{1}{\sqrt{2}} \begin{pmatrix} 1 & 1 \\ 1 & -1 \end{pmatrix}. \tag{2.29}$$

To construct a quantum computer, we need to implement the logical quantum gates using physical interactions. In the thesis, we will use the fidelity of states to compare the physical temporal evolution with an ideal quantum gate.

3 Dynamics of superconducting circuits

Throughout this thesis, we use the Jaynes–Cummings model developed originally in 1963 [28]. It describes a two-level system interacting with a quantized field of bosons. Although it was first derived for atoms and ions in a radiation field, the model can be applied to many other systems, including mesoscopic superconducting circuits. In this chapter, we briefly discuss how the mathematical representation of a specific quantum circuit can be cast in the form needed for the Jaynes–Cummings model.

3.1 Hamiltonian of the qubit

A superconducting qubit, traditionally referred to as the Cooper pair box, is essentially a small LC circuit with non-linear inductance arising from Josephson junctions. The Cooper pair box along with its circuit diagram is illustrated in Fig. 3.1. Below the critical temperature, the current in the circuit becomes supercurrent which is carried by electron–hole pairs, known as Cooper pairs [13].

A Josephson junction consists of two superconductors separated by a barrier that is thin enough for the Cooper pairs to cross via coherent quantum tunneling. The current I and voltage V_{q} across the junction are given by the Josephson equations [29]

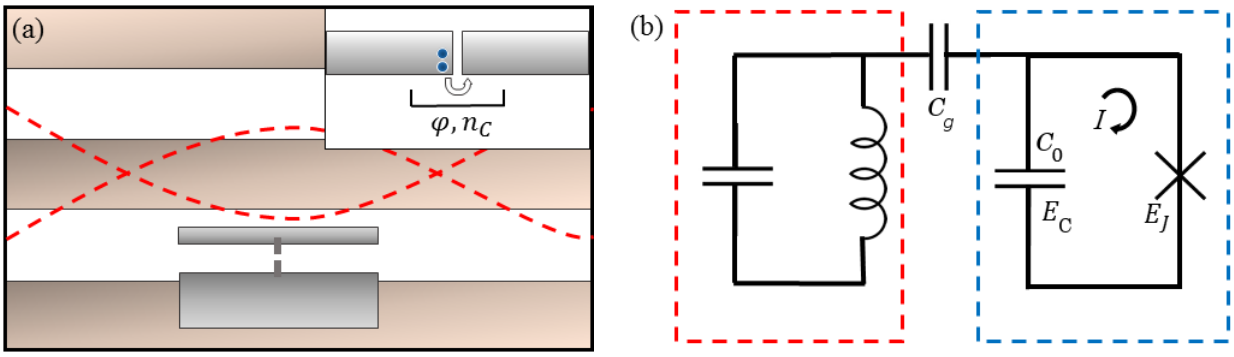

Figure 3.1: (a) Illustration of a superconducting qubit coupled to a superconducting resonator (gray and brown components, respectively). The inset shows a Josephson junction between two superconductors, with a Cooper pair crossing the junction. (b) Circuit diagram of the coupled system of the qubit and the resonator (blue and red boxes, respectively). The qubit consists of a capacitor and a Josephson junction, denoted by a cross. The symbols are defined in the main text.

$$I(t) = I_0 \sin\left[\varphi(t)\right], \tag{3.1}$$

$$V_{\mathrm{q}}(t) = \frac{\hbar}{2e}\frac{\partial\varphi}{\partial t}, \tag{3.2}$$

where I_0 is the so-called critical current of the junction, $\varphi = \varphi(t)$ is the phase difference of the electron wave functions across the junction, and $\hbar$ and e are the reduced Planck constant and elementary charge, respectively. The potential energy stored in the junction is given by

$$-\int V_{\mathrm{q}} I \mathrm{d}t = \frac{I_0\hbar}{2e}\cos\varphi. \tag{3.3}$$

In a Cooper pair box shown in Fig. 3.1b, energy is conservatively stored by a Josephson junction and a capacitor. Thus the Lagrangian describing the dynamics of the qubit can be expressed as

$$\begin{aligned}\mathcal{L} &= \frac{1}{2}C_0 V_q^2 + \frac{I_0\hbar}{2e}\cos\varphi \\ &= \frac{\hbar^2}{4E_{\mathrm{C}}}\left(\frac{\partial\phi}{\partial t}\right)^2 + E_{\mathrm{J}}\cos\varphi,\end{aligned} \tag{3.4}$$

where C_0 is the capacitance of the capacitor, and the scaling constants $E_{\mathrm{J}} = \hbar I_0/(2e)$ and $E_{\mathrm{C}} = (2e)^2/(2C_0)$ are known as the Josephson energy and the charging energy, respectively.

Let n_{C} denote the net number of Cooper pairs tunneled across a Josephson junction, carrying a charge $2e$. Neglecting a possible small charge offset caused by external couplings, the voltage of the capacitor is given by $V_{\mathrm{q}} = 2en_{\mathrm{C}}/C_0$, which combined with Eq. (3.2) yields

$$n_{\mathrm{C}} = \frac{\hbar}{2E_{\mathrm{C}}}\frac{\partial\varphi}{\partial t}. \tag{3.5}$$

The quantities $\hbar n_{\mathrm{C}}$ and φ are canonical conjugates, since

$$\frac{\partial\mathcal{L}}{\partial\left(\frac{\partial\varphi}{\partial t}\right)} = \frac{\hbar^2}{2E_{\mathrm{C}}}\frac{\partial\varphi}{\partial t} = \hbar n_{\mathrm{C}}. \tag{3.6}$$

The Hamiltonian of the qubit is therefore given by

$$H_{\mathrm{Q}} = \hbar n_{\mathrm{C}}\frac{\partial\varphi}{\partial t} - \mathcal{L} = E_{\mathrm{C}} n_{\mathrm{C}}^2 - E_{\mathrm{J}}\cos\varphi. \tag{3.7}$$

We invoke canonical quantization of the system by promoting the canonical conjugates

to operators $\hat{\varphi}$ and $\hat{n}_\mathrm{C}$. Furthermore, we define ladder operators $\hat{b}$ and $\hat{b}^\dagger$ such that

$$\hat{n}_\mathrm{C} = \left(\frac{E_\mathrm{J}}{2E_\mathrm{C}}\right)^{\frac{1}{4}} \frac{1}{\sqrt{2}} \left(\hat{b} + \hat{b}^\dagger\right), \tag{3.8}$$

$$\hat{\varphi} = i\left(\frac{E_\mathrm{J}}{2E_\mathrm{C}}\right)^{-\frac{1}{4}} \frac{1}{\sqrt{2}} \left(\hat{b}^\dagger - \hat{b}\right). \tag{3.9}$$

The operators $\hat{b}^\dagger$ and $\hat{b}$ create or annihilate an excitation of the qubit. Similar to the harmonic oscillator, they obey $[\hat{b}, \hat{b}^\dagger] = 1$ and the canonical commutation relation $[\hat{n}_\mathrm{C}, \hat{\varphi}] = i$ is satisfied.

The ratio $E_\mathrm{J}/E_\mathrm{C}$, which depends on the design of the circuit, determines whether the charging or the Josephson part dominates the dynamics [13]. Here, we use as an example the *transmon* qubit [30], a successful qubit type with a ratio $E_\mathrm{J}/E_\mathrm{C} \approx 100$, derived from the Cooper pair box. In this regime, it is shown in Ref. [30] that $\varphi \ll 1$ and thus the cosine in Eq. (3.7) may be approximated as $\cos\varphi \approx 1 - \varphi^2/2$. Inserting Eqs. (3.8) and (3.9) into (3.7) yields the approximate Hamiltonian

$$\hat{H}_\mathrm{Q} \approx \sqrt{2E_C E_\mathrm{J}} \left(\hat{b}^\dagger \hat{b} - \frac{1}{2}\hat{\mathbb{I}}\right) - E_\mathrm{J}\hat{\mathbb{I}}. \tag{3.10}$$

Due to the anharmonicity of the transmon, the oscillator can effectively occupy only the two lowest energy eigenstates, $|\mathrm{g}\rangle$ and $|\mathrm{e}\rangle$ [30]. Therefore the ladder operators can be approximated with $\hat{b}^\dagger \approx |\mathrm{e}\rangle\langle\mathrm{g}|$ and $\hat{b} \approx |\mathrm{g}\rangle\langle\mathrm{e}|$. After restricting to the two-level space, we may choose the zero point of energy such that

$$\hat{H}_\mathrm{Q} \approx \frac{1}{2}\sqrt{2E_C E_\mathrm{J}} \left(|\mathrm{e}\rangle\langle\mathrm{e}| - |\mathrm{g}\rangle\langle\mathrm{g}|\right). \tag{3.11}$$

It is customary to express this using the angular frequency ω_q corresponding to the transition energy of the qubit and the Pauli Z operator as

$$\hat{H}_\mathrm{Q} = -\frac{1}{2}\hbar\omega_\mathrm{q}\hat{\sigma}_\mathrm{z}. \tag{3.12}$$

3.2 Interaction with photons

Typically, the qubits are controlled by bosonic fields. In cQED, this can be achieved by coupling the qubit to a superconducting wave guide or a resonator. The supercurrent traveling in the wave guide induces an electromagnetic field outside it and, like any electromagnetic wave, it can be described by photons. The resonator is made so narrow that only longitu-

dinal modes can exist in it. We consider only the lowest mode with angular frequency ω. Using the number basis of Sec. 2.2, the free Hamiltonian of the driving resonator can be expressed as [23]

$$\hat{H}_{\mathrm{D}} = \hbar\omega\hat{a}^{\dagger}\hat{a}. \tag{3.13}$$

Here, we have removed the zero-point energy $\hbar\omega/2$ by choice of the energy reference.

Studying a circuit in which a qubit is capacitively coupled to a resonator, depicted in Fig. 3.1, yields a Hamiltonian with three distinct parts. In addition to the free Hamiltonians of the subsystems, $\hat{H}_{\mathrm{Q}}$ and $\hat{H}_{\mathrm{D}}$, the third part describing the interactions between the two is given by [31]

$$\hat{H}_{\mathrm{int}} = -C_{\mathrm{g}}\hat{V}_{\mathrm{q}} \otimes \hat{V}_{\mathrm{r}}, \tag{3.14}$$

where C_{g} is the capacitance of the coupling capacitor, $\hat{V}_{\mathrm{r}}$ is the voltage operator of the resonator, and $\hat{V}_{\mathrm{q}}$ is that of the qubit. The voltage in the resonator can be written as $\hat{V}_{\mathrm{r}} = V_{\mathrm{rms}}\left(\hat{a} + \hat{a}^{\dagger}\right)$, where V_{rms} is the root-mean-square voltage of a single photon [30]. The qubit voltage is given by

$$\hat{V}_{\mathrm{q}} = \frac{2e}{C_{\Sigma}}\hat{n}_{\mathrm{C}} = -\frac{\sqrt{2}e}{C_{\Sigma}}\left(\frac{E_{\mathrm{J}}}{2E_{\mathrm{C}}}\right)^{\frac{1}{4}}\left(\hat{b}^{\dagger} + \hat{b}\right). \tag{3.15}$$

Here, C_{Σ} is the total capacitance of the qubit and the coupling capacitor. Thus the interaction Hamiltonian is given by

$$\begin{aligned}\hat{H}_{\mathrm{int}} &= \sqrt{2}eV_{\mathrm{rms}}\frac{C}{C_{\Sigma}}\left(\frac{E_{\mathrm{J}}}{2E_{\mathrm{C}}}\right)^{\frac{1}{4}}\left(\hat{b} + \hat{b}^{\dagger}\right) \otimes \left(\hat{a} + \hat{a}^{\dagger}\right) \\ &\equiv \hbar g\left(\hat{b} + \hat{b}^{\dagger}\right) \otimes \left(\hat{a} + \hat{a}^{\dagger}\right),\end{aligned} \tag{3.16}$$

where all variables depending on the physical details have been combined into the *coupling constant* g. In the next chapter, the free Hamiltonians, $\hat{H}_{\mathrm{Q}}$ and $\hat{H}_{\mathrm{D}}$, and the interaction Hamiltonian, $\hat{H}_{\mathrm{int}}$, are used to derive the Jaynes–Cummings model.

We emphasize that effective Hamiltonians of the same form can be obtained for many different systems, not only for the superconducting transmon used here. For example, consider an atom in a cavity. The resonance frequencies can be chosen so that the atom can only make transitions between two energy levels. It interacts with the electric field $\hat{\mathbf{E}}$ through its dipole moment $\hat{\mathbf{d}}$ as $\hat{H}_{\mathrm{int}}^{\mathrm{atom}} = \hat{\mathbf{d}} \cdot \hat{\mathbf{E}}$. This can be similarly cast in the form of Eq. (3.16) [1, 32].

4 Quantum driving in the Jaynes–Cummings model

This chapter presents the physics of the Jaynes–Cummings model. We keep the system of interest on the abstract level, where a two-level system is driven by a quantized field of bosons. Section 4.1 completes the derivation of the Jaynes–Cummings Hamiltonian by invoking the rotating-wave approximation. In Sec. 4.2, this is used to calculate the complete temporal evolution of the system. Finally in Sec. 4.3, it is shown how the dynamics of this system manifest in a phenomenon known as Rabi oscillations, and how these oscillations can be used to control single qubits.

4.1 Rotating-wave approximation

We assume the coupled qubit–field system to be closed; we do not consider the noise and possible dissipative effects of an environment. The field is assumed to be monochromatic, a feature that is realized remarkably well in coplanar waveguides used in cQED. We only consider the resonant case where the transition energy of the qubit equals the energy of the photons. This assumption greatly simplifies our analysis. For a more general treatment, one would define a detuning parameter as the difference between the qubit energy gap and the photon energy. A treatment with detuning can be found in, e.g., Refs. [33, 14].

The Hilbert space of the combined system is a tensor product of that of the two-level system and the Fock space, $\mathcal{H} = \mathcal{H}_\mathrm{Q} \otimes \mathcal{H}_\mathrm{D}$. The Hamiltonian consists of the free Hamiltonians of the individual systems and the additional part describing their interaction

$$\hat{H} = \hat{H}_\mathrm{Q} \otimes \hat{\mathbb{I}}_\mathrm{D} + \hat{\mathbb{I}}_\mathrm{Q} \otimes \hat{H}_\mathrm{D} + \hat{H}_\mathrm{int}, \tag{4.1}$$

where $\hat{\mathbb{I}}$ is the identity operator of the respective spaces. As demonstrated in Ch. 3, they are given by

$$\begin{aligned}
\hat{H}_\mathrm{Q} &= \frac{\hbar\omega}{2}\left(|\mathrm{e}\rangle\langle\mathrm{e}| - |\mathrm{g}\rangle\langle\mathrm{g}|\right) && (4.2)\\
\hat{H}_\mathrm{D} &= \hbar\omega\hat{a}^\dagger\hat{a} && (4.3)\\
\hat{H}_\mathrm{int} &= \hbar g\left(\hat{b}^\dagger \otimes \hat{a} + \hat{b} \otimes \hat{a}^\dagger + \hat{b}^\dagger \otimes \hat{a}^\dagger + \hat{b} \otimes \hat{a}\right). && (4.4)
\end{aligned}$$

with $\hat{b} = |\mathrm{g}\rangle\langle\mathrm{e}|$. For general treatment, we assume that the coupling g has temporal dependence.

Note that $\hat{H}_\mathrm{int}$ contains terms of two types. The first two terms contain a creation operator and an annihilation operator, corresponding to energy transfer between the qubit

and the field. The remaining terms involve two operators that increase or decrease the energy of both subsystems. By transforming the system into an interaction picture with respect to the free Hamiltonian $\hat{H}_0 = \hat{H}_\mathrm{Q} \otimes \hat{\mathbb{I}}_\mathrm{D} + \hat{\mathbb{I}}_\mathrm{Q} \otimes \hat{H}_\mathrm{D}$, we show that the last two terms in Eq. (4.4) can be neglected if $\omega \gg g$. In the interaction picture, all operators are transformed as [23]

$$\hat{A} \to \hat{A}^\mathrm{I} = \mathrm{e}^{i\hat{H}_0 t/\hbar} \hat{A} \mathrm{e}^{-i\hat{H}_0 t/\hbar}, \tag{4.5}$$

where

$$\mathrm{e}^{i\hat{H}_0 t/\hbar} = \mathrm{e}^{i\left(\hat{H}_\mathrm{Q}\otimes\hat{\mathbb{I}}_\mathrm{D} + \hat{\mathbb{I}}_\mathrm{Q}\otimes\hat{H}_\mathrm{D}\right)t/\hbar} = \mathrm{e}^{i\hat{H}_\mathrm{Q} t/\hbar} \otimes \mathrm{e}^{i\hat{H}_\mathrm{D} t/\hbar}. \tag{4.6}$$

The transformed operators are denoted by a superscript I. The purpose of the transformation in Eq. (4.5) is to switch into a coordinate system in the Hilbert space that is co-moving with the natural free evolution of the system.

The exponentiations of the free Hamiltonians $\hat{H}_\mathrm{Q}$ and $\hat{H}_\mathrm{D}$, defined in Eqs. (4.2) and (4.3), can be calculated by standard matrix exponentiation, yielding

$$\mathrm{e}^{i\hat{H}_\mathrm{Q} t/\hbar} = \mathrm{e}^{-i\omega t/2} |\mathrm{g}\rangle\langle\mathrm{g}| + \mathrm{e}^{i\omega t/2} |\mathrm{e}\rangle\langle\mathrm{e}|, \tag{4.7}$$

$$\mathrm{e}^{i\hat{H}_\mathrm{D} t/\hbar} = \mathrm{e}^{i\omega \hat{N} t}. \tag{4.8}$$

According to Eq. (4.5), the annihilation operators transform as

$$\hat{b}^\mathrm{I} = \mathrm{e}^{i\hat{H}_\mathrm{Q} t/\hbar}\, \hat{b}\, \mathrm{e}^{-i\hat{H}_\mathrm{Q} t/\hbar} = \mathrm{e}^{-i\omega t} \hat{b}, \tag{4.9}$$

$$\hat{a}^\mathrm{I} = \mathrm{e}^{i\omega \hat{N} t}\, \hat{a}\, \mathrm{e}^{-i\omega \hat{N} t} = \mathrm{e}^{-i\omega t} \hat{a}. \tag{4.10}$$

Thus the transformed interaction Hamiltonian is given by

$$\begin{aligned} \hat{H}^\mathrm{I}_\mathrm{int} &= \mathrm{e}^{i\hat{H}_0 t/\hbar} \hat{H}_\mathrm{int} \mathrm{e}^{-i\hat{H}_0 t/\hbar} \\ &= \hbar g \left[\left(\hat{b}^\mathrm{I}\right)^\dagger \otimes \hat{a}^\mathrm{I} + \hat{b}^\mathrm{I} \otimes \left(\hat{a}^\mathrm{I}\right)^\dagger + \left(\hat{b}^\mathrm{I}\right)^\dagger \otimes \left(\hat{a}^\mathrm{I}\right)^\dagger + \hat{b}^\mathrm{I} \otimes \hat{a}^\mathrm{I} \right] \\ &= \hbar g \left(\hat{b}^\dagger \otimes \hat{a} + \hat{b} \otimes \hat{a}^\dagger + \mathrm{e}^{2i\omega t} \hat{b}^\dagger \otimes \hat{a}^\dagger + \mathrm{e}^{-2i\omega t} \hat{b} \otimes \hat{a} \right). \end{aligned} \tag{4.11}$$

We observe that in this frame, the energy transfer terms are stationary, i.e., co-rotating with the frame, whereas the remaining, so-called counter-rotating terms oscillate with frequencies $\pm 2\omega$. If $\omega \gg g$, the effect of the counter-rotating terms averages to out in the natural time scale of the first terms [32]. For this reason, we neglect the counter-rotating terms. By making this *rotating-wave approximation*, we arrive at the Jaynes–Cummings

Hamiltonian

$$\hat{H}_{\text{int}}^{\text{I}} = \hbar g \left(\hat{b}^\dagger \otimes \hat{a} + \hat{b} \otimes \hat{a}^\dagger \right) \widehat{=} \hbar g \begin{pmatrix} 0 & \hat{a}^\dagger \\ \hat{a} & 0 \end{pmatrix}. \tag{4.12}$$

For the matrix notation, we use the basis defined in Eq. (2.3). The Hamiltonian (4.12) was first derived by Jaynes and Cummings [28] and it is the usual starting point of many studies. The rotating-wave approximation offers significant simplifications in the following derivations, altough some analytical results can be derived without it. A more general model without the rotating-wave approximation is generally referred to as the Rabi model [34].

4.2 Temporal evolution

Having simplified the Hamiltonian into the Jaynes–Cummings form, we are able to analytically solve the complete dynamics of the system. We denote the density operators of the qubit and the field by $\hat{\chi}$ and $\hat{\sigma}$, respectively, and the operator of the whole system by $\hat{\rho} = \hat{\chi} \otimes \hat{\sigma}$.

In the interaction picture, the temporal evolution is determined by [23]

$$i\hbar \frac{\mathrm{d}}{\mathrm{d}t} \hat{\rho}^{\text{I}}(t) \;=\; \left[\hat{H}_{\text{int}}^{\text{I}}(t),\, \hat{\rho}^{\text{I}}(t) \right]. \tag{4.13}$$

This is equivalent to the von Neumann equation involving the original Hamiltonian [Eq. (2.17)]. The equivalence can be shown by inserting the definition of the transformed density operator of Eq. (4.5) into Eq. (4.13). From this point on, the superscripts will be omitted as we will work in the interaction picture only. As discussed in Sec. 2.3, the solution of Eq. (4.13) is $\hat{\rho}(t) = \hat{U}(t)\hat{\rho}(0)\hat{U}^\dagger(t)$, where the unitary operator is given by

$$\hat{U}(t) = \exp\left[-i \int_0^t \hat{H}_{\text{int}}(t')dt'/\hbar \right]. \tag{4.14}$$

The only part of $\hat{H}_{\text{int}}$ with possible temporal dependence is $g(t)$ which results in the integral $\int_0^t g(t')dt'$. For simplicity, we choose to use a constant interaction strength, for which $\int_0^t g(t')dt' = gt$, but a more general treatment can be reobtained by making the substitution $gt \to \int_0^t g(t')dt'$ below.

An explicit form of the temporal evolution operator is computed by writing the exponent as a sum of matrices and separating the even and odd summations. Using the matrix

representation for operators in $\mathcal{H}_{\mathrm{Q}}$, $\hat{U}(t)$ is expressed as

$$\begin{aligned}\hat{U}(t) &\widehat{=} \exp\left[-igt\begin{pmatrix}0 & \hat{a}^\dagger\\ \hat{a} & 0\end{pmatrix}\right] = \sum_{n=0}^{\infty}\frac{(-igt)^n}{n!}\begin{pmatrix}0 & \hat{a}^\dagger\\ \hat{a} & 0\end{pmatrix}^n\\ &= \sum_{n=0}^{\infty}\frac{(-igt)^{2n}}{2n!}\begin{pmatrix}0 & \hat{a}^\dagger\\ \hat{a} & 0\end{pmatrix}^{2n} + \sum_{n=0}^{\infty}\frac{(-igt)^{2n+1}}{(2n+1)!}\begin{pmatrix}0 & \hat{a}^\dagger\\ \hat{a} & 0\end{pmatrix}^{2n+1}. \end{aligned} \tag{4.15}$$

The matrix powers can be computed using Eqs. (2.5) and (2.4). For example

$$\begin{aligned}\begin{pmatrix}0 & \hat{a}^\dagger\\ \hat{a} & 0\end{pmatrix}^{2n} &= \begin{pmatrix}\left(\hat{a}^\dagger\hat{a}\right)^n & 0\\ 0 & \left(\hat{a}\hat{a}^\dagger\right)^n\end{pmatrix} = \begin{pmatrix}\sum_k \hat{N}^n\left|k\right\rangle\left\langle k\right| & 0\\ 0 & \sum_k\left(\hat{N}+1\right)^n\left|k\right\rangle\left\langle k\right|\end{pmatrix}\\ &= \sum_{k=0}^{\infty}\begin{pmatrix}\left(\sqrt{k}\right)^{2n}\left|k\right\rangle\left\langle k\right| & 0\\ 0 & \left(\sqrt{k+1}\right)^{2n}\left|k\right\rangle\left\langle k\right|\end{pmatrix}, \end{aligned} \tag{4.16}$$

and similarly for the matrix with powers of $2n+1$. Combining these leads to

$$\begin{aligned}\hat{U}(t) &\widehat{=} \sum_{n,k=0}^{\infty}\begin{pmatrix}\frac{1}{2n!}\left(-igt\sqrt{k}\right)^{2n}\left|k\right\rangle\left\langle k\right| & \frac{1}{(2n+1)!}\left(-igt\sqrt{k+1}\right)^{2n+1}\left|k+1\right\rangle\left\langle k\right|\\ \frac{1}{(2n+1)!}\left(-igt\sqrt{k}\right)^{2n+1}\left|k-1\right\rangle\left\langle k\right| & \frac{1}{2n!}\left(-igt\sqrt{k+1}\right)^{2n}\left|k\right\rangle\left\langle k\right|\end{pmatrix}\\ &= \sum_{k=0}^{\infty}\begin{pmatrix}\cos\left(gt\sqrt{k}\right)\left|k\right\rangle\langle k| & -i\sin\left(gt\sqrt{k+1}\right)\left|k+1\right\rangle\langle k|\\ -i\sin\left(gt\sqrt{k}\right)\left|k-1\right\rangle\langle k| & \cos\left(gt\sqrt{k+1}\right)\left|k\right\rangle\langle k|\end{pmatrix}. \end{aligned} \tag{4.17}$$

Introducing the shorthand notations $C^k = \cos\left(gt\sqrt{k}\right)$ and $S^k = \sin\left(gt\sqrt{k}\right)$, the temporal evolution operator can be expressed as

$$\hat{U}(t)\widehat{=}\sum_{k=0}^{\infty}\begin{pmatrix}C^k\left|k\right\rangle\langle k| & -iS^{k+1}\left|k+1\right\rangle\langle k|\\ -iS^k\left|k-1\right\rangle\langle k| & C^{k+1}\left|k\right\rangle\langle k|\end{pmatrix}. \tag{4.18}$$

Given an initial state $\hat{\rho}(0) = \hat{\rho}_0 = \hat{\chi}_0 \otimes \hat{\sigma}_0$, the evolving state is given by

$$\hat{\rho}(t) = \hat{U}(t)\left(\hat{\chi}_0 \otimes \hat{\sigma}_0\right)\hat{U}^\dagger(t). \tag{4.19}$$

The reduced qubit and field density operators are obtained by using the partial traces as

$$\hat{\chi}(t) = \mathrm{Tr}_{\mathrm{D}}\hat{\rho}(t), \quad \hat{\sigma}(t) = \mathrm{Tr}_{\mathrm{Q}}\hat{\rho}(t)\ . \tag{4.20}$$

Note that the temporal evolution of $\hat{\rho} \in \mathcal{H}$ is unitary, as the evolution of closed system

should be. On the other hand, in general there is no unitary evolution operator for the separate components $\hat{\chi} \in \mathcal{H}_{\mathrm{Q}}$ and $\hat{\sigma} \in \mathcal{H}_{\mathrm{D}}$. As mentioned in Ch. 2.3, this means that initially pure components do not necessarily remain pure. The loss of purity is caused by the entanglement of the qubit and the field, causing some of the qubit information to be transferred to the field.

4.3 Quantum driving

Controlling the state of a qubit with a quantized auxiliary system is here referred to as quantum driving. For purposes of quantum computing, quantum driving with the Jaynes–Cummings interaction is used to implement logical quantum gates. In this section, we specifically focus on the NOT gate which exchanges the states $|\mathrm{e}\rangle \leftrightarrow |\mathrm{g}\rangle$. This gate is represented with the Pauli matrix σ_{x}.

What parameters can we manipulate to drive the qubit? The dynamics of the qubit are determined by three components: the temporal evolution operator, the initial state of the qubit, and that of the auxiliary system which we refer to as the drive. The state of the qubit does not offer any free parameters since during a quantum computation the qubit is generally in an unknown state. That is, we cannot adjust the gate depending on the input. The evolution operator offers one parameter: the interaction time t (more precisely, the dimensionless time gt) which can be chosen as needed. Finally, the initial state of the drive, being an element of the Fock space, offers infinitely many degrees of freedom. In summary, implementing a NOT gate corresponds to constructing a suitable drive state with a matching interaction time. In the following sections of this chapter, we study some example cases commonly found in the literature: Rabi oscillations and quantum driving in the classical limit.

4.3.1 Rabi oscillations

A qubit coupled to a drive typically exhibits oscillations between the ground and the excited state. This well-known effect arising from the Jaynes–Cummings interaction is known as Rabi oscillation [14, 32] and it has been observed experimentally with superconducting qubits [35]. An extreme and purely quantum mechanical case is the vacuum Rabi oscillation, where coupling the qubit to a vacuum state causes it to oscillate. To study how Rabi oscillation comes about, let the initial states be $\hat{\chi}_0 = |\mathrm{g}\rangle\langle\mathrm{g}|$ and $\hat{\sigma}_0 = |n\rangle\langle n|$. The evolving

state is given by Eq. (4.19), which simplifies to

$$\begin{aligned}\hat{\rho}(t) &\mathrel{\widehat{=}} \sum_{k,j=0}^{\infty} \begin{pmatrix} C^k\,|k\rangle\langle k| & -iS^{k+1}\,|k+1\rangle\langle k| \\ -iS^k\,|k-1\rangle\langle k| & C^{k+1}\,|k\rangle\langle k| \end{pmatrix} \\ &\quad \times \begin{pmatrix} |n\rangle\langle n| & 0 \\ 0 & 0 \end{pmatrix} \begin{pmatrix} C^j\,|j\rangle\langle j| & iS^j\,|j\rangle\langle j-1| \\ iS^{j+1}\,|j\rangle\langle j+1| & C^{j+1}\,|j\rangle\langle j| \end{pmatrix} \\ &= \begin{pmatrix} C^nC^n\,|n\rangle\langle n| & iS^nC^n\,|n\rangle\langle n-1| \\ -iS^nC^n\,|n-1\rangle\langle n| & S^nS^n\,|n-1\rangle\langle n-1| \end{pmatrix}. \end{aligned} \tag{4.21}$$

To compute the evolving components, the partial trace equations (4.20) are used to obtain

$$\hat{\chi}(t) = \cos^2\left(gt\sqrt{n}\right)|\mathrm{g}\rangle\langle\mathrm{g}| + \sin^2\left(gt\sqrt{n}\right)|\mathrm{e}\rangle\langle\mathrm{e}|\,, \tag{4.22}$$

$$\hat{\sigma}(t) = \cos^2\left(gt\sqrt{n}\right)|n\rangle\langle n| + \sin^2\left(gt\sqrt{n}\right)|n-1\rangle\langle n-1|\,, \tag{4.23}$$

showing the dynamically oscillating nature of the states.

The dynamics can be interpreted as the qubit coherently emitting a photon to the resonator and re-absorbing it, periodically *ad infinitum*. The excitation probability is simply $P_\mathrm{e} = \sin^2(gt\sqrt{n})$. Using an interaction time $t = \pi/(2g\sqrt{n})$ leads to $P_\mathrm{e} = 1$, i.e., a complete flip of the state. Thus we have demonstrated that the perfect state transformation $|\mathrm{g}\rangle \to |\mathrm{e}\rangle$ is implementable simply using a number state $|n\rangle$. However, this does not serve as a perfect NOT gate, for example, because the excited state evolves with a frequency proportional to $\sqrt{n+1}$. That is, the two basis states $\{|\mathrm{g}\rangle, |\mathrm{e}\rangle\}$ couple to different number states and therefore rotate with different frequencies. In the extreme case of $n = 0$, the excited state would oscillate normally but the ground state would not evolve at all. In the next sections, we consider more complex initial states which may be used to implement a NOT gate.

4.3.2 Classical driving

The classical treatment of driving is notably simpler than the quantum driving discussed above. In the non-quantized description for the electromagnetic field, one replaces the ladder operators with complex numbers $a_\mathrm{cl} = |a_\mathrm{cl}|\,\mathrm{e}^{i\varphi}$ in Eq. (4.4) [36]. The complex number φ represents the phase difference between the oscillations of the qubit and the field. In the rotating-wave approximation with an amplitude a_cl, the interaction Hamiltonian and the temporal evolution operator become

$$\hat{H}_\mathrm{cl} \mathrel{\widehat{=}} \hbar g \begin{pmatrix} 0 & a_\mathrm{cl}^* \\ a_\mathrm{cl} & 0 \end{pmatrix}, \tag{4.24}$$

$$\hat{U}_{\mathrm{cl}}(t) \;\widehat{=}\; \begin{pmatrix} \cos\left(gt\,|a_{\mathrm{cl}}|\right) & -i\mathrm{e}^{-i\varphi}\sin\left(gt\,|a_{\mathrm{cl}}|\right) \\ -i\mathrm{e}^{i\varphi}\sin\left(gt\,|a_{\mathrm{cl}}|\right) & \cos\left(gt\,|a_{\mathrm{cl}}|\right) \end{pmatrix}. \tag{4.25}$$

Since the classical field is not considered to be part of the Hilbert space, the evolving qubit is simply $\hat{\chi}(t) = \hat{U}_{\mathrm{cl}}(t)\hat{\chi}_0\hat{U}_{\mathrm{cl}}^{\dagger}(t)$. With the choice $t = \pi/(2g\,|a_{\mathrm{cl}}|)$, the evolution operator reduces to $i\hat{U}_{\mathrm{cl}} = \cos(\varphi)\hat{\sigma}_{\mathrm{x}} + \sin(\varphi)\hat{\sigma}_{\mathrm{y}}$. Thus the gates corresponding to $\hat{\sigma}_{\mathrm{x}}$ and $\hat{\sigma}_{\mathrm{y}}$ are implemented by choosing the appropriate interaction time and phase of the pulse. In the common nomenclature, this choice of interaction time is referred to as the π pulse. A π pulse rotates the Bloch vector by π about the chosen axis—a classical π pulse with $\varphi = 0$ implements a perfect NOT gate. However, the semi-classical description of Eq. (4.25) is not always accurate. To this end, take the above example of Rabi oscillations applied to the vacuum by setting $a_{\mathrm{cl}} = 0$. This leads to $\hat{U}_{\mathrm{cl}}(t) = \hat{\mathbb{I}}$, i.e., there is no oscillation at all in the classical case, even though the dynamics of the excited state are non-trivial in the full quantum treatment.

4.3.3 Quantum driving in the classical limit

The case of the classical drive offers a hint towards a good NOT gate. We need to find a drive state that, in some sense, approaches the classical drive. This is commonly taken to be the coherent state $|\mathrm{D}_\alpha\rangle$ [Eq. (2.7)] in the limit of infinite photons, $\overline{n} = |\alpha|^2 \to \infty$ [36].

The quantum evolution of a ground-state qubit, coupled to the coherent drive state $\hat{\sigma}_0 = \left|\mathrm{D}_{\sqrt{\overline{n}}}\right\rangle\!\left\langle D_{\sqrt{\overline{n}}}\right|$ is illustrated in Fig. 4.1. The excitation probability is computed as $P_{\mathrm{e}}(t) = \langle \mathrm{e}|\,\hat{\chi}(t)\,|\mathrm{e}\rangle$, where $\hat{\chi}(t)$ is given by Eqs. (4.20) and (4.19). For comparison, the semi-classical evolution is also shown using Eq. (4.25). We observe that the coherent states induce oscillations similar to those arising from the classical field. Specifically, the case of $\overline{n} = |a_{\mathrm{cl}}|^2$ matches the classical evolution. This observation suggests that the classical state may be approximated by the coherent states, although the oscillations are damped in time[2]. To achieve an optimal NOT gate, we need to stop the evolution when the probability reaches its first local maximum. This corresponds to the π rotation. Due to the damping, the following maxima are always lower than the first one, indicating a less precise state transformation.

In the following, we show more rigorously how the dynamics with the coherent state

[2]The oscillation of the excited-sate probability seems to collapse to a static value of 50%, but after a certain time the oscillations appear again (not shown in Fig. 4.1). This phenomenon is known as the revival of the oscillation which has been studied extensively, see Refs. [36, 14, 32]. The theory of collapses and revivals is beyond the scope of this thesis.

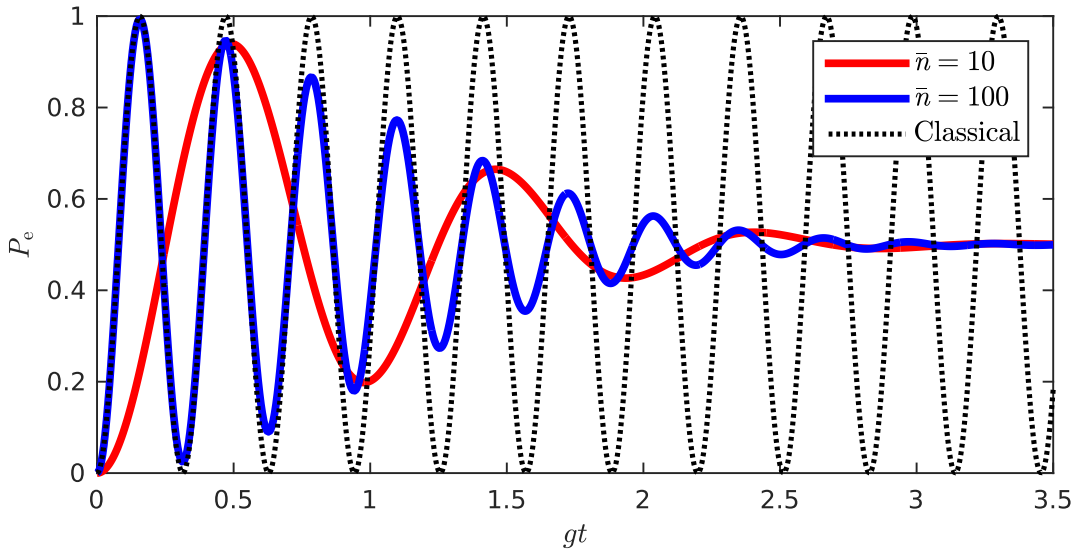

Figure 4.1: Probability P_e to observe the qubit in the excited state as a function of dimensionless time gt. At $t = 0$ the qubit is in the ground state. The two solid lines correspond to the initial drive being in a coherent state with an average photon number of 10 (red) and 100 (blue). The dashed line corresponds to the system evolving according to the classical Hamiltonian with a field amplitude $a_{cl} = 10$.

reduce to those with the classical drive in the proper limit. First, we choose a different basis for the qubit space, defined by [36]

$$|\pm\rangle = \frac{1}{\sqrt{2}} \left(|g\rangle \pm |e\rangle \right). \tag{4.26}$$

These basis states are eigenstates of $\hat{H}_{cl}$ in Eq. (4.24). Their usefulness emerges when coupled to a coherent state

$$\left|D_{\sqrt{\bar{n}}}\right\rangle = e^{-\bar{n}/2} \sum_n \frac{\bar{n}^{\,n/2}}{\sqrt{n!}} |n\rangle . \tag{4.27}$$

The temporal evolution of the combined state $|\pm\rangle \otimes \left|D_{\sqrt{\bar{n}}}\right\rangle$ has been calculated in Ref. [36] in the classical limit of large $\bar{n}$. Explicitly, their lengthy calculation shows that

$$\left[|\pm\rangle \otimes \left|D_{\sqrt{\bar{n}}}\right\rangle \right](t) = \frac{1}{\sqrt{2}} \left[e^{-i\frac{gt}{2\sqrt{\bar{n}}}} |g\rangle \pm |e\rangle \right] \otimes e^{-\bar{n}/2} \sum_n \frac{\bar{n}^{\,n/2}}{\sqrt{n!}} e^{\pm igt\sqrt{\bar{n}}} |n\rangle . \tag{4.28}$$

The most notable feature is that, besides gaining additional factors, the state vector accurately stays in the factorized form throughout the evolution.

To implement a NOT gate, we use a carefully chosen interaction time

$$t^* = \frac{\pi}{2g\sqrt{\overline{n}}}. \tag{4.29}$$

This corresponds exactly to the first local extremum in Fig. (4.1). Evaluated at t^*, Eq. (4.28) reduces to

$$\begin{aligned}\left[|\pm\rangle \otimes \left|\mathrm{D}_{\sqrt{\overline{n}}}\right\rangle\right](t^*) &= \frac{1}{\sqrt{2}}\left[\mathrm{e}^{-\frac{i\pi}{4\overline{n}}}|\mathrm{g}\rangle \pm |\mathrm{e}\rangle\right] \otimes \mathrm{e}^{-\overline{n}/2}\sum_n \frac{\overline{n}^{n/2}}{\sqrt{n!}}\mathrm{e}^{\pm i\pi/2}|n\rangle \\ &= \pm i\,|\pm\rangle \otimes \left|\mathrm{D}_{\sqrt{\overline{n}}}\right\rangle, \end{aligned} \tag{4.30}$$

in the limit $\overline{n} \to \infty$. The $|\pm\rangle$ states gain a phase factor of $\pm i$. Switching back to the energy basis and denoting the evolved states with an asterisk, we obtain

$$\begin{aligned} |\pm^*\rangle &= \pm i\,|\pm\rangle \\ \Rightarrow \frac{1}{\sqrt{2}}\left(|\mathrm{g}^*\rangle \pm |\mathrm{e}^*\rangle\right) &= i\frac{1}{\sqrt{2}}\left(\pm|\mathrm{g}\rangle + |\mathrm{e}\rangle\right) \\ \Rightarrow \begin{cases} |\mathrm{g}^*\rangle &= i\,|\mathrm{e}\rangle \\ |\mathrm{e}^*\rangle &= i\,|\mathrm{g}\rangle\,. \end{cases} \end{aligned} \tag{4.31}$$

Apart from the redundant phase i, the basis states are exchanged without error, as in the case of a classical Hamiltonian. Thus the coherent state, in the limit $\overline{n} \to \infty$, can be used to reproduce the classical results.

The remaining question is, what happens in the region of finite $\overline{n}$. As demonstrated in Fig. 4.1, decreasing the mean photon number of a coherent state increases the error of the NOT gate. Furthermore, there is no fundamental reason why the coherent state would yield the highest fidelity for a given $\overline{n}$. Perhaps there are other states that could outperform the coherent state with only a couple of photons. What is the most optimal state? In the following chapter, we develop powerful tools to access these questions and to show that indeed, the coherent state is not the optimal choice, even in the limit of large $\overline{n}$.

5 Drive state optimization

In the previous chapter, we showed that a large coherent state can be used to implement a NOT gate. Here, we present a new approach to study which drive states are suitable for different logical operations. When comparing the fidelity of possible logical gates, we need to take into account that the state transformation fidelity depends on the input state. Since the input values are generally unknown during the computation, a consistent way to compare gates is to assess their minimum state fidelities, that is, the fidelity of the worst possible input. In this thesis, the minimum fidelity is referred to as the *gate fidelity* [1]. The higher the gate fidelity is, the more precisely all inputs are guaranteed to be transformed. This is essential for error correction codes, in which any gate error must be under the tolerance threshold. Another input-independent measure for gate performance is the average transformation fidelity, which is discussed in Sec. 6.4.

5.1 Gate fidelity

Let the function F measure the fidelity of a given state transformation realized by the Jaynes–Cummings interaction. Here, F depends on the initial state of the qubit and that of the drive, denoted by $\hat{\chi}_0 \in \mathcal{H}_\mathrm{Q}$ and $\hat{\sigma}_0 \in \mathcal{H}_\mathrm{D}$, respectively. The gate fidelity is denoted by F_min and the worst-case qubit by $\hat{\chi}_\mathrm{w}$. The problem is to find the optimal drive state $\hat{\sigma}_\mathrm{opt}$ that maximizes the gate fidelity, so that

$$F_\mathrm{min}(\hat{\sigma}_\mathrm{opt}) = \max_{\hat{\sigma}_0} F\left(\hat{\chi}_\mathrm{w}, \hat{\sigma}_0\right) = \max_{\hat{\sigma}_0} \min_{\hat{\chi}_0} F\left(\hat{\chi}_0, \hat{\sigma}_0\right). \tag{5.1}$$

In addition, we are most interested in solutions that consist of as few photons as possible.

Let $\hat{\chi}_{U}(t)$ denote the state resulting from the physical interaction, and $\hat{\chi}_{K}$ the ideally transformed qubit. By the results of the previous chapter, the evolving qubit state is expressed as

$$\hat{\chi}_{U}(t) = \mathrm{Tr}_\mathrm{D}\left[\hat{U}(t)\left(\hat{\chi}_0 \otimes \hat{\sigma}_0\right)\hat{U}^\dagger(t)\right], \tag{5.2}$$

where $\hat{U}(t)$ is given by Eq. (4.18). The ideal target state is given by $\hat{\chi}_{K} = \hat{K}\hat{\chi}_0\hat{K}^\dagger$, where $\hat{K} = \hat{K} \otimes \hat{\mathbb{I}}$ is the operator corresponding to the desired single-qubit gate. Using the definitions given in Ch. 2, the fidelity is given by

$$F\left[\hat{\chi}_{U}(t), \hat{\chi}_{K}\right] = \mathrm{Tr}_\mathrm{Q}\left[\hat{\chi}_{U}(t)\hat{\chi}_{K}\right]. \tag{5.3}$$

5.1.1 Minimization with pure states

Due to the properties of the gate fidelity, the density operator formalism reduces to that of the pure states. Here, we show that a pure drive state yielding the highest gate fidelity cannot be surpassed by a mixed state. Let $\hat{\sigma}_0$ be an arbitrary initial drive state and express it using the expansion in Eq. (2.15) as

$$\hat{\sigma}_0 = \sum_{i \neq \text{opt}} p_i \left|\sigma_i\right\rangle\!\left\langle\sigma_i\right| + \left(1 - \sum_{i \neq \text{opt}} p_i\right) \left|\sigma_{\text{opt}}\right\rangle\!\left\langle\sigma_{\text{opt}}\right|. \tag{5.4}$$

Here, $\left|\sigma_{\text{opt}}\right\rangle\!\left\langle\sigma_{\text{opt}}\right|$ denotes the state yielding the highest gate fidelity among all pure states. Since $\hat{\chi}_U$ and F are linear in $\hat{\sigma}_0$, we observe that

$$\begin{aligned} F_{\min}(\hat{\sigma}_0) &= \sum_{i \neq \text{opt}} p_i F_{\min}\left(\left|\sigma_i\right\rangle\!\left\langle\sigma_i\right|\right) + (1 - \sum_{i \neq \text{opt}} p_i) F_{\min}\left(\left|\sigma_{\text{opt}}\right\rangle\!\left\langle\sigma_{\text{opt}}\right|\right) \\ &= F_{\min}\left(\left|\sigma_{\text{opt}}\right\rangle\!\left\langle\sigma_{\text{opt}}\right|\right) + \sum_{i \neq \text{opt}} p_i \left[F_{\min}\left(\left|\sigma_i\right\rangle\!\left\langle\sigma_i\right|\right) - F_{\min}\left(\left|\sigma_{\text{opt}}\right\rangle\!\left\langle\sigma_{\text{opt}}\right|\right)\right] \end{aligned} \tag{5.5}$$

By the assumption that $\left|\sigma_{\text{opt}}\right\rangle\!\left\langle\sigma_{\text{opt}}\right|$ produces the highest fidelity among pure states, the expression in the square brackets is never positive. Thus we have $F_{\min}(\hat{\sigma}_0) \leq F_{\max}\left(\left|\sigma_{\text{opt}}\right\rangle\!\left\langle\sigma_{\text{opt}}\right|\right)$, showing that a mixed drive state cannot produce a gate fidelity higher than the optimal pure state.

A similar result holds for the mixed qubits, which is shown in Ref. [1]. The proof is based on the fact that fidelity is a jointly concave function. Thus we conclude that a solution to Eq. (5.1) can be found by considering pure states only.

5.1.2 State transformation fidelity with pure states

With pure initial states $\hat{\chi}_0 \otimes \hat{\sigma}_0 \equiv \left|\chi_0\right\rangle\!\left\langle\chi_0\right| \otimes \left|\sigma_0\right\rangle\!\left\langle\sigma_0\right| \equiv \left|\chi_0, \sigma_0\right\rangle\!\left\langle\chi_0, \sigma_0\right|$, Eq. (5.3) simplifies into

$$\begin{aligned} F\left[\hat{\chi}_U(t), \hat{\chi}_K\right] &= \text{Tr}_{\text{Q}}\left[\hat{\chi}_U(t)\hat{\chi}_K\right] \\ &= \text{Tr}_{\text{Q}}\left\{\text{Tr}_{\text{D}}\left[\hat{U}(t)\left(\hat{\chi}_0 \otimes \hat{\sigma}_0\right)\hat{U}^\dagger(t)\right]\hat{K}\hat{\chi}_0\hat{K}^\dagger\right\} \\ &= \left\langle\chi_0\right|\hat{K}^\dagger \text{Tr}_{\text{D}}\left[\hat{U}(t)\left|\chi_0, \sigma_0\right\rangle\left\langle\chi_0, \sigma_0\right|\hat{U}^\dagger(t)\right]\hat{K}\left|\chi_0\right\rangle \\ &= \sum_{k=0}^{\infty} \left\langle\chi_0, k\right|\hat{K}^\dagger\hat{U}(t)\left|\chi_0, \sigma_0\right\rangle\left\langle\chi_0, \sigma_0\right|\hat{U}^\dagger(t)\hat{K}\left|\chi_0, k\right\rangle \end{aligned}$$

$$= \sum_{k=0}^{\infty} \left| \langle \chi_0, k | \hat{K}^\dagger \hat{U}(t) | \chi_0, \sigma_0 \rangle \right|^2 \equiv \sum_k |G_k|^2 . \tag{5.6}$$

Here $\langle \chi_0, k| \equiv \langle \chi_0| \otimes \langle k|$ and we have denoted the final matrix elements by $\{G_k\}$.

To obtain an explicit expression for the matrix element G_k, we define the initial drive state $|\sigma_0\rangle$ and initial qubit state $|\chi_0\rangle$ as

$$|\sigma_0\rangle = \sum_{j=0}^{\infty} c_j |j\rangle, \tag{5.7}$$

$$|\chi_0\rangle \mathrel{\hat{=}} \begin{pmatrix} \sqrt{1-|z|^2} \\ z \end{pmatrix}. \tag{5.8}$$

The coefficients $\{c_j\}$ are complex numbers that are normalized to unity, $\sum_j |c_j|^2 = 1$. The qubit state is completely determined by the complex parameter z. Using these definitions and Eq. (4.18), the matrix element G_k can be written as

$$\begin{aligned}
G_k &= \langle \chi_0, k | \hat{K}^\dagger \hat{U}(t) | \chi_0, \sigma_0 \rangle \\
&= \sum_{l=0}^{\infty} \sum_{j=0}^{\infty} \begin{pmatrix} \sqrt{1-|z|^2}\langle k| & z^* \langle k| \end{pmatrix} \begin{pmatrix} K_{11} & K_{12} \\ K_{21} & K_{22} \end{pmatrix}^\dagger \\
&\qquad \times \begin{pmatrix} C^l |l\rangle\langle l| & -iS^{l+1} |l+1\rangle\langle l| \\ -iS^l |l-1\rangle\langle l| & C^{l+1} |l\rangle\langle l| \end{pmatrix} \begin{pmatrix} \sqrt{1-|z|^2} c_j |j\rangle \\ z c_j |j\rangle \end{pmatrix} \\
&= \sum_{j=0}^{\infty} \begin{pmatrix} \sqrt{1-|z|^2} & z^* \end{pmatrix} \begin{pmatrix} K_{11}^* & K_{21}^* \\ K_{12}^* & K_{22}^* \end{pmatrix} \\
&\qquad \times \begin{pmatrix} C^k \delta_{jk} & -iS^k \delta_{j,k-1} \\ -iS^{k+1} \delta_{j,k+1} & C^{k+1} \delta_{jk} \end{pmatrix} \begin{pmatrix} \sqrt{1-|z|^2} \\ z \end{pmatrix} c_j \\
&= \sum_{j=0}^{\infty} c_j \Big\{ -iS^{k+1} \delta_{j,k+1} \left[K_{12} \left(1-|z|^2\right) + K_{22}^* z^* \sqrt{1-|z|^2} \right] \\
&\qquad\qquad -iS^k \delta_{j,k-1} \left[K_{12}^* |z|^2 + K_{11}^* z \sqrt{1-|z|^2} \right] \\
&\qquad\qquad +C^{k+1} \delta_{jk} \left[K_{22}^* |z|^2 + K_{12} z \sqrt{1-|z|^2} \right] \\
&\qquad\qquad +C^k \delta_{jk} \left[K_{11}^* \left(1-|z|^2\right) + K_{12}^* z^* \sqrt{1-|z|^2} \right] \Big\}
\end{aligned}$$

$$= \sum_{mn=0}^{1} \Gamma_{nm}^{k} c_{k+n-m}. \tag{5.9}$$

In the last line, the sum has been structured to separate the amplitudes $\{c_k\}$ from the other factors $\left\{\Gamma_{nm}^{k}\right\}$ that depend on the initial qubit value z, the desired gate $\hat{K}$, and time t. Explicitly,

$$\Gamma_{mn}^{k}(z,t,\hat{K}) = \begin{pmatrix} C^k\left[K_{11}^*\left(1-|z|^2\right)+K_{12}^* z^*\sqrt{1-|z|^2}\right] & -iS^k\left[K_{12}^*|z|^2+K_{11}^* z\sqrt{1-|z|^2}\right] \\ -iS^{k+1}\left[K_{21}^*\left(1-|z|^2\right)+K_{22}^* z^*\sqrt{1-|z|^2}\right] & C^{k+1}\left[K_{22}^*|z|^2+K_{21}^* z\sqrt{1-|z|^2}\right] \end{pmatrix}_{nm}. \tag{5.10}$$

In summary, the fidelity of the state transformation can be evaluated with

$$F\left(z,\sigma_0,t,\hat{K}\right) = \sum_k |G_k|^2 = \sum_k \left| \sum_{mn=0}^{1} \Gamma_{nm}^{k}(z,t,\hat{K}) c_{k+n-m} \right|^2. \tag{5.11}$$

5.2 Maximizing the state fidelity

With expression (5.11), we are able to solve the optimization problem of Eq. (5.1) which is equivalent to finding the critical points of F. The most straightforward procedure would be to calculate the gradient of F with respect to all degrees of freedom, $\{c_j\}$, z, and t. Unfortunately, equating the gradient to zero yields a complex system of nonlinear equations. However, with some reasoning z and t may be kept constant during the optimization with respect to $\{c_j\}$. This leads to a systematic technique to construct the optimal drive states.

In Ch. 4, we solved the dynamics for a coherent drive state and then chose an appropriate interaction time t^* optimal for a π rotation. Below however, we want to compare arbitrary drive states which may produce their optimal results with different interaction times. To make the comparison of states consistent, we fix the interaction time. Furthermore, solving Eq. (5.1) does not require including z in the gradient if the point of minimum fidelity is found by other means. This is possible with certain restrictions, detailed in the Sec. 6.1; here, we assume that we have already found the qubit value z that minimizes the fidelity and that it does not depend on $\{c_j\}$.

With z, $\hat{K}$, and t constant, we solve $\nabla F\left(z,\sigma_0,t,\hat{K}\right) = 0$, where the gradient is computed with respect to the coefficients $\{c_j\}$ of the drive state $|\sigma_0\rangle$. In addition, the normalization constraint $\sum_j |c_j|^2 = 1$ must be satisfied. Applying the method of Lagrange multipliers, we set out to solve the following equation:

$$\nabla\left[F\left(\{c_j\}\right) - \lambda\left(\sum_j |c_j|^2 - 1\right)\right] = 0. \tag{5.12}$$

Here, λ is the Lagrange multiplier of the constraint and $F(\{c_j\})$ is given by Eq. (5.11). The solutions of this equation represent the critical points of F in the Fock space.

We write the complex-valued amplitudes using two real numbers as $c_j = x_j + iy_j$ and compute the gradient piece by piece. Using Eq. (5.9) we obtain

$$\nabla G_k = \sum_{j=0}^{\infty} \sum_{mn=0}^{1} \Gamma^k_{nm} \delta_{k,j+m-n} \nabla c_j = \sum_{j=0}^{\infty} \sum_{mn=0}^{1} \Gamma^k_{nm} \delta_{k,j+m-n} \left(\hat{\mathbf{x}}_j + i\hat{\mathbf{y}}_j\right), \tag{5.13}$$

and hence

$$\begin{aligned} \nabla F(\{c_j\}) &= \nabla \sum_k |G_k|^2 = \sum_k \left(\nabla G_k^*\right) G_k + \text{c.c.} \\ &= \sum_k \sum_{jl} \sum_{mnm'n'} \left(\Gamma^k_{nm}\right)^* \Gamma^k_{n'm'} \delta_{k,l+m'-n'} \delta_{k,j+m-n} \left(\hat{\mathbf{x}}_j - i\hat{\mathbf{y}}_j\right) c_l + \text{c.c.} \\ &= \sum_{jl} A_{jl} \left(\hat{\mathbf{x}}_j - i\hat{\mathbf{y}}_j\right) c_l + \text{c.c.}, \end{aligned} \tag{5.14}$$

where c.c. denotes the complex conjugate of the preceding expression, and we defined

$$A_{jl} = \sum_{mnm'n'} \left(\Gamma^{j+m-n}_{nm}\right)^* \Gamma^{j+m-n}_{n'm'} \delta_{l+m'-n',j+m-n\geq 0}, \tag{5.15}$$

which can be considered as the elements of a Hermitian matrix $A(z,t) = [A_{jl}]$.

Thus Eq. (5.12) reads

$$\sum_{jl} A_{jl} \left(\hat{\mathbf{x}}_j - i\hat{\mathbf{y}}_j\right) c_l + \text{c.c.} - \lambda \sum_j \left(2x_j \hat{\mathbf{x}}_j + 2y_j \hat{\mathbf{y}}_j\right) = 0. \tag{5.16}$$

By the orthogonality of the unit vectors $\hat{\mathbf{x}}_j$ and $\hat{\mathbf{y}}_j$, we obtain

$$\begin{cases} \sum_l A_{jl} c_l + \text{c.c.} = 2\lambda x_j \\ -i \sum_l A_{jl} c_l + \text{c.c.} = 2\lambda y_j \end{cases} \forall j, \tag{5.17}$$

whence

$$\begin{aligned} 2\sum_l A_{jl} c_l &= 2\lambda x_j + 2\lambda i y_j, \quad \forall j \\ \sum_l A_{jl} c_l &= \lambda c_j, \quad \forall j. \end{aligned} \tag{5.18}$$

This is an eigenvalue equation for the matrix A defined in Eq. (5.15). Since the eigenvectors

of A represent the critical points in the Fock space, one of the eigenvectors, $|\sigma_{\text{opt}}\rangle$, gives the global maximum of the fidelity.

Furthermore, the eigenvalues equal the fidelity produced by the corresponding drive states. To show this, we rescale the solved coefficients with a real number ξ as $\left\{c_j^\lambda\right\} \to \left\{\xi c_j^\lambda\right\}$. Since the fidelity is quadratic in $\left\{c_j^\lambda\right\}$, the Lagrange equation optimizing the fidelity with respect to ξ yields

$$\frac{\partial}{\partial \xi}\left[\xi^2 F\left(\left\{c_j^\lambda\right\}\right) - \lambda\left(\sum_j \xi^2 \left|c_j^\lambda\right|^2 - 1\right)\right] = 0$$

$$\Rightarrow F\left(\left\{c_j^\lambda\right\}\right) = \lambda \sum_j \left|c_j^\lambda\right|^2 = \lambda. \tag{5.19}$$

Hence the greatest fidelity, corresponding to that of the optimal drive state, equals the largest eigenvalue.

Note that the eigenvalue equation can be generalized for multiple values $z_1, z_2, ...z_N$ to find the maximum of $\frac{1}{N}\sum_p^N F(z_p)$. Repeating the above procedure, we observe that the modified equation

$$\nabla\left[\frac{1}{N}\sum_{p=1}^{N} F(z_p) - \lambda\left(\sum_j |c_j|^2 - 1\right)\right] = 0 \tag{5.20}$$

leads to

$$\sum_l \left[\frac{1}{N}\sum_{p=1}^{N} A_{jl}(z_p, t)\right] c_l = \lambda c_j, \quad \forall j. \tag{5.21}$$

Thus $A(z,t)$ can be replaced with $\frac{1}{N}\left[A(z_1,t) + A(z_2,t) + ... + A(z_N,t)\right]$ to compute the drive state that optimizes the fidelity averaged over multiple qubit states.

6 Optimal drive states

In this chapter, the optimization method developed in the previous section is used to discover the drive states that maximize the gate fidelity of a NOT gate and perform rotations more accurately than their coherent counterparts, even in the classical limit. Section 6.2 shows how the optimal states can be approximated accurately by a superposition of squeezed coherent states. Similar results are obtained for the π rotation about the y-axis, as discussed in Sec. 6.3. Using these approximations in Ch. 7, we are able to calculate the theoretical upper bound of the NOT gate fidelity.

6.1 Numerically exact solutions for the NOT gate

In Sec. 5.2, we showed that the transformation fidelity of a given qubit can be maximized with a proper choice of the drive state. However, optimizing the drive state using a fixed input qubit state generally causes other input states to transform with smaller fidelities. This problem can be avoided if the worst-case qubit z_{w}, defined by $F(z_{\mathrm{w}}) = \min_z F(z)$, does not depend on the drive state. After finding such z_{w}, the fidelity $F(z_{\mathrm{w}})$ can be maximized by applying Eq. (5.21) and hence solving Eq. (5.1).

It turns out that for gates corresponding to the operators $\hat{\sigma}_{\mathrm{x}}$ and $\hat{\sigma}_{\mathrm{y}}$, there is a symmetry that causes z_{w} to be independent of the drive state. In this section, we study the NOT gate, $\hat{K} = \hat{\sigma}_{\mathrm{x}}$, as a representative case. This choice simplifies Eq. (5.10) into

$$\Gamma^k_{mn}(z,t) = \begin{pmatrix} C^k z^* \sqrt{1-|z|^2} & -iS^k |z|^2 \\ -iS^{k+1}\left(1-|z|^2\right) & C^{k+1} z \sqrt{1-|z|^2} \end{pmatrix}_{nm}. \tag{6.1}$$

In appendix A, it is shown that for real $\{c_j\}$ and interaction time $t \leq \pi/(2g)$, the worst-case qubit for the NOT gate is either $z_{\mathrm{w}} = ir$ or $z_{\mathrm{w}} = -ir$, with $r \approx 1/\sqrt{2}$. However, maximizing $F(ir)$ causes $F(-ir)$ to decrease and vice versa. Therefore, the optimal state is given by an equation that maximizes the sum $F(ir) + F(-ir)$. Applying Eq. (5.21), this sum is maximized by the solution of

$$\sum_l \frac{1}{2}\left[A\left(\frac{+i}{\sqrt{2}}, t\right) + A\left(\frac{-i}{\sqrt{2}}, t\right)\right]_{jl} c_l \;=\; \lambda c_j, \quad \forall j, \tag{6.2}$$

where $A(z,t)$ is given by Eqs. (5.15) and (6.1). We do not attempt to solve this matrix equation analytically. However, approximate analytical solutions are discussed in Sec. 6.2. Numerically, the eigenvectors of Eq. (6.2) can be solved conveniently. Picking the states

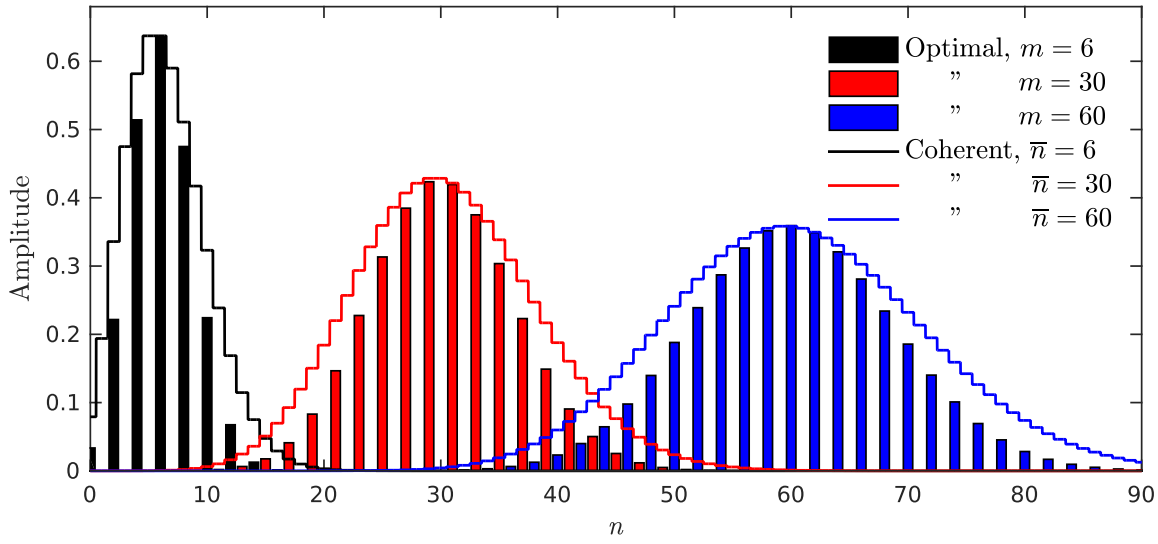

Figure 6.1: Amplitudes of photon number states in optimal drive states for times $t = \pi/(2g\sqrt{m})$ with $m = 6$, 30, 60 (black, red, and blue bars respectively). For comparison, coherent states (solid lines) of average photon number $\overline{n} = 6$, 30, 60 are shown and rescaled to the same height.

corresponding to the largest eigenvalues, the optimal drive states are obtained for a chosen time t. Examples of the solutions are illustrated in Fig. 6.1. Several distinct features are observed:

- The optimal state $|\sigma_{\rm opt}(t)\rangle$ resembles the coherent state $\left|\mathrm{D}_{\sqrt{\overline{n}}}\right\rangle$ with $t = \pi/\left(2g\sqrt{\overline{n}}\right)$. This equals the π rotation time t^* introduced in Sec. 4.3.3.

- In an optimal state, only even or odd number states are occupied. For each even state there is an equivalent odd state with equal eigenvalue and resulting fidelity.

- The optimal states appear to be squeezed. The exact amount of squeezing is studied in Sec. 7.1.

We conclude that the optimal states are modified versions of the usual coherent states. These properties hold for any interaction time $t \leq \pi/(2g)$. For the worst-case qubit value $z = \pm ir$ we used the convenient $r = 1/\sqrt{2} \approx 0.7$. However, solving the optimal drive states using values between $r = 0.6...0.8$ yields drive states that are nearly identical with the ones obtained with $r = 1/\sqrt{2}$. The difference in the resulting gate fidelities is less than 10^{-4} for only 25 average photons.

The gate fidelity with an optimal drive state is higher than that with the corresponding coherent state. This is demonstrated in Fig. 6.2. If the initial state is a coherent state $|\mathrm{D}_{\pm\alpha}\rangle$,

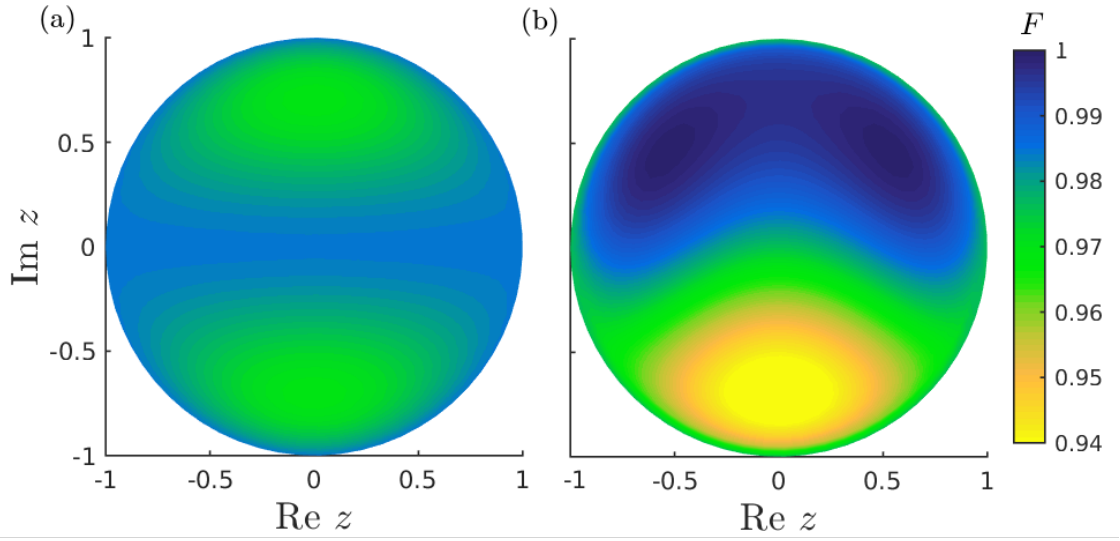

Figure 6.2: Fidelity of the NOT gate as a function of the input qubit value z. The ground state, the north pole of the Bloch sphere, is located at the origin ($z = 0$); the excited state corresponds to the whole outer circumference ($|z|^2 = 1$). (a) The initial drive state is chosen to maximize the sum $F(i/\sqrt{2}) + F(-i/\sqrt{2})$ at time $t = \pi/\left(2g\sqrt{25}\right)$. (b) The initial drive state is a coherent state of real amplitude corresponding to the same t as in (a). The fidelities averaged over the spheres are 0.979 and 0.977 for panels (a) and (b), respectively.

the fidelity is very high around $z = \pm i/\sqrt{2}$ but not impressive around $z = \mp i/\sqrt{2}$. If the optimal drive state is used, such deep values are elevated, resulting in a higher minimum fidelity on the Bloch sphere.

Why does the combination of modifications listed above yield the optimal solution? A heuristic explanation could be that the gate error accumulates from two sources: the uncertainty of the drive energy and the entanglement between the two subsystems. The optimal state balances these two sources. It is not surprising that the optimal states are similar to the coherent ones which are known to implement a NOT gate of rather high fidelity, as discussed in Sec. 4.3.3. With a squeezed coherent state, the number distribution peaks more strongly around the number state that matches the chosen π pulse time.

On the other hand, strong entanglement reduces the purity of the qubit, inevitably increasing error. The amount of entanglement can be deduced by comparing the drive states after the interaction with either the ground state or the excited state as the initial qubit state. The interaction with the ground or the excited state reduces or increases the number of photons by one, respectively. If we are able to distinguish between these alternatives by measuring the resulting drive state, information has clearly been transferred in the form of entanglement. This explains why squeezing the state only helps up to a certain point. A significantly squeezed state is strongly peaked around the mean value, rendering the removal

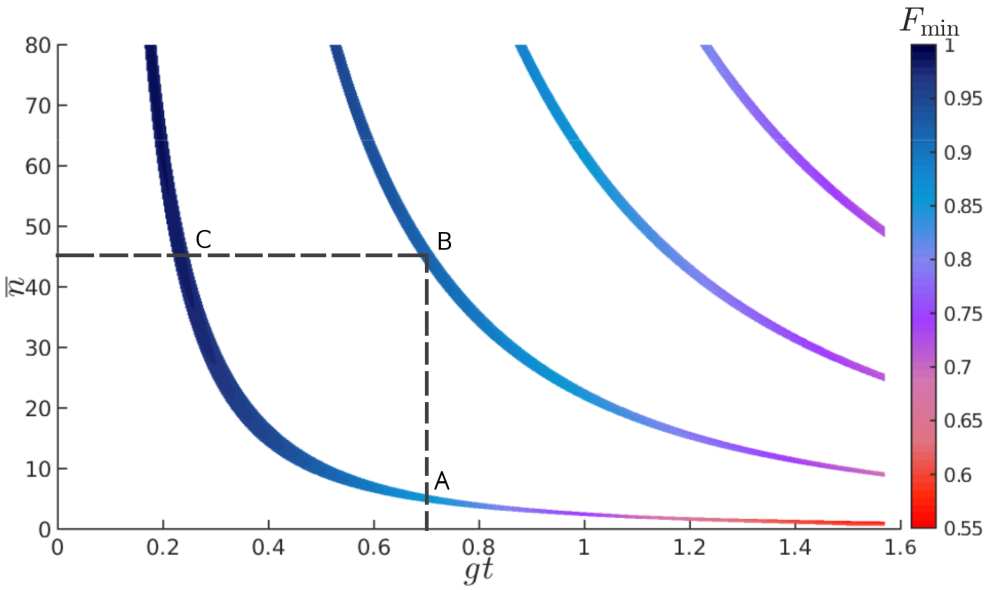

Figure 6.3: Average number of photons $\overline{n}$ in an optimal drive state for dimensionless interaction time gt. The color indicates the minimum fidelity $F_{\min}$ of a NOT gate with corresponding optimal state and interaction time. Each curve is a family of optimal solutions. The states represented by the higher curves are identical with those of the curve nearest to the origin. For example, the points A and B represent solutions for a given time t. The point B does not represent a fundamentally new solution since it is identical to the state represented by point C, only further in the oscillation cycle.

or addition of a photon clearly observable. On the other hand, removing all even or odd photon states from a coherent distribution does not increase entanglement: an even drive state state evolves into an odd state regardless of the initial qubit state.

Note that the dimension of the Fock space is infinite and hence A has an infinite amount of eigenvectors. Increasing the size of the matrix A and solving Eq. (6.2) for time t yields drive states similar to the first solution, but with a higher mean photon number. For an infinite-sized A, the optimal state would therefore seem to have an infinite amount of photons. This behavior has been illustrated in Fig. 6.3. However, the additional solutions are redundant; for these drive states, the given value of t is not the point of the first maximum of fidelity oscillation. The same solutions are found with briefer interaction times, yielding even higher gate fidelity. Thus without loss of generality, we may restrict our studies to the family of solutions corresponding to the first maximum, hence removing the ambiguity of states corresponding to a fixed choice of t.

6.2 Approximate optimal states

Above, we solved the problem of finding the optimal drive states for the NOT gate. However, our solutions are only a set of numbers that satisfy the eigenvalue equation. To study their characteristics, it is useful to have the solutions in a closed analytic form.

6.2.1 Squeezed cat states

Guided by the observations in Sec. 6.1, we guess that the exact solutions can be approximated very accurately by a certain superposition of squeezed states. The approximate solutions should have the shape of a squeezed state and a well-defined parity, i.e., they should contain only even or odd number states.

First, we use the squeezing operator $\hat{\mathcal{S}}(s)$ to obtain a squeezed coherent state

$$\left|\mathrm{S}_{\alpha}^{(s)}\right\rangle = \hat{\mathcal{D}}\left(\alpha\right)\hat{\mathcal{S}}(s)\left|0\right\rangle, \tag{6.3}$$

introduced in Sec. 2.2.1. Second, we note that the parity property can be realized with a superposition of coherent states of opposite phase as

$$\begin{aligned}\frac{1}{\sqrt{N}}\left[\hat{\mathcal{D}}(\alpha)\pm\hat{\mathcal{D}}(-\alpha)\right]\left|0\right\rangle &= \frac{1}{\sqrt{N}}\left[\left|\mathrm{D}_{\alpha}\right\rangle\pm\left|\mathrm{D}_{-\alpha}\right\rangle\right]\\ &= \frac{1}{\sqrt{N}}\sum_{n=0}^{\infty}\frac{1}{\sqrt{n!}}\left[\alpha^{n}\pm(-\alpha)^{n}\right]\left|n\right\rangle\\ &= \frac{1}{\sqrt{N}}\sum_{n=\substack{\text{even}\\\text{odd}}}\frac{1}{\sqrt{n!}}\alpha^{n}\left|n\right\rangle.\end{aligned} \tag{6.4}$$

Here the normalization factor is $N = 2\left(1\pm\exp(-2|\alpha|^{2})\right)$ and the last sum involves either even or odd numbers, depending on the sign in the superposition. This configuration is commonly referred to as the *cat state* [20]. In the Wigner representation, the state exhibits two Gaussian shapes centered at α and $-\alpha$, with small interference near the origin. The amplitude of the interference vanishes with increasing α.

Combining these two features, our ansatz for the approximate solution, which one may refer to as the squeezed cat state, is thus

$$\left|\Sigma_{\alpha}^{\pm}\right\rangle = \frac{1}{\sqrt{\tilde{N}}}\left(\left|\mathrm{S}_{\alpha}^{(s)}\right\rangle\pm\left|\mathrm{S}_{-\alpha}^{(s)}\right\rangle\right), \tag{6.5}$$

where $\tilde{N}$ is the normalization coefficient and the squeezing parameter s is to be determined. In Sec. 7.1, it is shown to be $s = \frac{1}{2}\ln\frac{\pi}{2}$. The above ansatz coincides with the numerically

obtained optimal drive state as α increases, which verifies that the optimal drive state for $\overline{n} \gg 1$ is a squeezed cat state. For example, the overlap of the exact solution and the approximation is $|\langle\sigma_{\text{opt}}\,|\,\Sigma_\alpha\rangle|^2 \approx 1 - 10^{-4}$ and the difference between the resulting gate fidelities is $F_{\min}(|\sigma_{\text{opt}}\rangle) - F_{\min}(|\Sigma_\alpha\rangle) \approx 10^{-5}$ in the case of only $\overline{n} = |\alpha|^2 = 25$ photons.

Note that a single coherent state $|\mathrm{D}_{\pm\alpha}\rangle$ with real α rotates the Bloch vector clockwise or anticlockwise about the x-axis, depending on the sign of α. Thus in the optimal drive state, the superposition of components rotating the vector in different directions results in a constructive interference after a full rotation by π. This is the main reason why the optimal drive state produces a better fidelity than a single coherent state; the effect of squeezing is not as significant.

6.2.2 Normal distribution

A closed analytic form of the optimal coefficients is obtained by considering the squeezed cat state $|\Sigma_\alpha^\pm\rangle$ in the limit $\alpha \to \infty$. The photon number in the squeezed states obeys the Poisson distribution $\mathcal{P}(n)$ with the mean and variance given by Eqs. (2.11) and (2.12). Assuming large $|\alpha|$ and real squeezing parameter s, the moments are approximately $\overline{n} \approx |\alpha|^2$ and $\nu^2 \approx |\alpha|^2 \mathrm{e}^{-2s}$.

In the limit of large $\overline{n}$, the Poisson distribution coincides with the normal distribution

$$\mathcal{P}(n) \approx \frac{1}{\sqrt{2\pi}\nu} \exp\left[-\frac{(n-\overline{n})^2}{2\nu^2}\right]. \tag{6.6}$$

Thus the occupation probabilities of the squeezed state can be approximated with

$$|c_n(\alpha,s)|^2 \;\approx\; \frac{1}{\sqrt{2\pi}\,|\alpha|\,\mathrm{e}^{-s}} \exp\left[-\frac{(n-|\alpha|^2)^2}{2\,|\alpha|^2\,\mathrm{e}^{-2s}}\right]. \tag{6.7}$$

To include even number states only, we multiply this by a factor $\cos^2(\pi n/2)$ which equals 0 for odd n and 1 for even n. The odd state is obtained with $\sin^2(\pi n/2)$. After proper rescaling, the amplitudes of the optimal state $|\Sigma_\alpha^+\rangle = \sum_n \tilde{c}_n\,|n\rangle$ are given by

$$\tilde{c}_n \;=\; \sqrt{2}\left(2\pi\mathrm{e}^{-2s}\right)^{-1/4} \alpha^{-1/2} \exp\left[-\frac{\mathrm{e}^{2s}}{4}\left(\frac{n}{\alpha}-\alpha\right)^2\right] \cos^2\left(\frac{\pi k}{2}\right),\;\; \alpha \to \infty. \tag{6.8}$$

6.3 Additional gates

The NOT gate is not the only single-qubit gate that benefits from our optimization techniques. The optimal drive state for the Pauli Y rotation or for the $\pi/2$ rotations about x-

Table 6.1: Optimal implementations of rotation gates, with a given α. Decimal values are obtained from numerical analysis. The gate fidelities are given for drive states with $\overline{n} = 25$.

Gate	$\sigma_{\mathrm{x}}(\pi)$	$\sigma_{\mathrm{y}}(\pi)$	$\sigma_{\mathrm{x}}(\pm\pi/2)$	$\sigma_{\mathrm{y}}(\pm\pi/2)$
Worst-case qubit	$i/\sqrt{2}$	$1/\sqrt{2}$	$\mp 0.93i$	± 0.93
Optimal state	$\left\|\mathrm{S}_{\alpha}^{(s)}\right\rangle \pm \left\|\mathrm{S}_{-\alpha}^{(s)}\right\rangle$	$\left\|\mathrm{S}_{i\alpha}^{(s)}\right\rangle \pm \left\|\mathrm{S}_{-i\alpha}^{(s)}\right\rangle$	$\left\|\mathrm{S}_{\pm\alpha}^{(s)}\right\rangle$	$\left\|\mathrm{S}_{\pm i\alpha}^{(s)}\right\rangle$
Squeezing parameter s	$\frac{1}{2}\ln\frac{\pi}{2}$	$-\frac{1}{2}\ln\frac{\pi}{2}$	0.058	-0.058
Interaction time	$\pi/(2\alpha)$	$\pi/(2\alpha)$	$\pi/(4\alpha)$	$\pi/(4\alpha)$
Gate fidelity of optimal state	0.9692	0.9692	0.9781	0.9781
Gate fidelity of coherent state	0.9355	0.9355	0.9780	0.9780

and y-axes can be solved by replacing the Pauli operator $\hat{\sigma}_{\mathrm{x}}$ with $\hat{\sigma}_{\mathrm{y}}$, $\sqrt{\hat{\sigma}_{\mathrm{x}}}$, or $\sqrt{\hat{\sigma}_{\mathrm{y}}}$ in the above analysis. After the worst-case qubit has been identified and used to carry out the optimization, the resulting optimal states are approximated with squeezed (cat) states. The results for different rotations about axes in the xy-plane are shown in Table 6.1. For example, the worst-case qubits for the Pauli Y gate are given by $z_{\mathrm{w}} \approx \pm 1/\sqrt{2}$ and the resulting optimal states resemble the squeezed cat state $\left|\mathrm{S}_{i\alpha}^{(s)}\right\rangle \pm \left|\mathrm{S}_{-i\alpha}^{(s)}\right\rangle$. This is consistent with the classical case of driving considered in Sec. 4.3.3, where the Y rotation was achieved with an amplitude $\pm i\alpha$. The fidelity on the Bloch sphere is identical to that shown in Fig. 6.2, but rotated by 90 degrees. The minimum and average fidelities for optimal X and Y gates are equal for a given $\overline{n}$. On the other hand, the $\pi/2$ rotations are readily optimized with drive states that are very close to the non-squeezed coherent states.

Other gates, such as the Pauli Z gate and the Hadamard gate which can be constructed using a combination of rotations about the x- and y-axes, cannot be optimized directly by our method. For these gates, the worst-case qubit depends strongly on the initial drive state and therefore a high minimum fidelity cannot be guaranteed. The optimization method assumes a single drive state for the whole interaction, whereas the Pauli Z and Hadamard gates constructed using the X and Y rotations require at least two different drive states for the sequential interactions. The Pauli Z gate can also be implemented by a non-resonant dispersive pulse, but it is beyond the scope of this thesis.

6.4 Average state fidelity

The optimization method of the previous chapter can be used to solve a drive state that maximizes the average state fidelity instead of the gate fidelity. Assuming the qubit obeys a uniform probability distribution on the surface of the Bloch sphere, the fidelity averaged over all qubit states is given by

$$\overline{F}(\sigma_0, t) = \frac{1}{4\pi} \int_0^{\pi} \int_0^{2\pi} F(z, \sigma_0, t, \hat{K}) \, \sin\theta \, \mathrm{d}\phi \mathrm{d}\theta, \tag{6.9}$$

where F is the fidelity given by Eq. (5.11) and $z = \sin(\theta/2)\, \mathrm{e}^{i\phi}$. Evaluation of the integral for the NOT gate yields

$$\begin{aligned} \overline{F}(\sigma_0, t) &= \frac{1}{3} + \frac{1}{6} \sum_k \left\{ |c_k|^2 \left[\sin^2\left(gt\sqrt{k}\right) + \sin^2\left(gt\sqrt{k+1}\right) \right] \right. \\ &\quad \left. + 2 \sin\left(gt\sqrt{k}\right) \sin\left(gt\sqrt{k+1}\right) \mathrm{Re}\left(c_{k+1} c_{k-1}^*\right) \right\}, \end{aligned} \tag{6.10}$$

where $\{c_k\}$ are the drive state coefficients.

We optimize $\overline{F}$ using the method developed in Sec. 5.2. In this case, the Lagrange multiplier equation leads to an eigenvalue equation $\sum_l B_{jl} c_l = \lambda c_j$, where the matrix B is given by

$$\begin{aligned} B_{jk} &= \frac{1}{6} \left\{ \left[\sin^2\left(gt\sqrt{k}\right) + \sin^2\left(gt\sqrt{k+1}\right) \right] \delta_{jk} + \sin\left(gt\sqrt{k+2}\right) \sin\left(gt\sqrt{k+1}\right) \delta_{l,k+2} \right. \\ &\quad \left. + \sin\left(gt\sqrt{k}\right) \sin\left(gt\sqrt{k-1}\right) \delta_{l,k-2} \right\}. \end{aligned} \tag{6.11}$$

For small interaction times ($gt \ll \pi/2 \Leftrightarrow \overline{n} \gg 1$), the states that optimize the two quantities, $F_{\min}$ and $\overline{F}$, coincide. Thus the previously discovered squeezed cat state $|\Sigma^{\pm}\rangle$ not only maximizes the gate fidelity, but the average state fidelity as well. Note that this way, the optimal state is reobtained without the assumption of real drive coefficients that was made in Sec. 6.1.

The difference between the average fidelity of the coherent state and the optimal state is rather small. Thus using the optimal drive state instead of the coherent state improves the minimum fidelity while essentially preserving the average.

7 Upper bound of NOT gate fidelity

With all the tools developed in the previous chapters, we are able to elaborate on the original problem of finding

$$F_{\min}(\overline{n}) = \max_{\sigma_0} \min_{\chi_0} F\left[\chi_0, \sigma_0(\overline{n})\right]. \tag{7.1}$$

The gate fidelity $F_{\min}(\overline{n})$ is limited by an upper bound $F_{\mathrm{b}}(\overline{n})$ which is reached with the worst-case qubit and the optimal state. The worst-case qubit $\chi_{\mathrm{w}}(z)$ for the NOT gate is given by $z \approx i/\sqrt{2}$ and the optimal state is expressed as $|\sigma_{\mathrm{opt}}(t)\rangle = \sum_n \tilde{c}_n(t)\,|n\rangle$. With these states, the fidelity [Eq. (5.11)] becomes

$$\begin{aligned}
F_{\mathrm{b}}(t) &= \sum_k \left| \langle \chi_{\mathrm{w}}, k|\, \hat{K}^\dagger \hat{U}(t)\, |\chi_{\mathrm{w}}, \sigma_{\mathrm{opt}}(t)\rangle \right|^2 \\
&= \frac{1}{4}\sum_k \left| \langle k| \begin{pmatrix} -i & 1 \end{pmatrix} \hat{U}(t) \begin{pmatrix} 1 \\ i \end{pmatrix} |\sigma_{\mathrm{opt}}(t)\rangle \right|^2 \\
&= \frac{1}{4}\sum_k \left| \sum_{l=0}^{\infty} \langle k| \left(-iC^l\,|l\rangle\langle l| - iS^{l+1}\,|l+1\rangle\langle l| - iS^l\,|l-1\rangle\langle l| + iC^{l+1}\,|l\rangle\langle l| \right) |\sigma_{\mathrm{opt}}(t)\rangle \right|^2 \\
&= \frac{1}{4}\sum_k \left| \tilde{c}_k(t) \left[\cos\left(\sqrt{k}t\right) - \cos\left(\sqrt{k+1}t\right) \right] + \tilde{c}_{k-1}(t) \sin\left(\sqrt{k}t\right) + \tilde{c}_{k+1}(t) \sin\left(\sqrt{k+1}t\right) \right|^2 .
\end{aligned}$$

Using trigonometric identities, the parity property $\tilde{c}_k \tilde{c}_{k\pm1} = 0$, and an interaction time $t = \pi/\left(2g\sqrt{\overline{n}}\right)$ corresponding to a π rotation, the expression becomes

$$\begin{aligned}
F_{\mathrm{b}}(\overline{n}) &= \frac{1}{2} + \frac{1}{2}\sum_n \left\{ \tilde{c}_{n+1}\tilde{c}_{n-1} \sin\left(\frac{\pi}{2}\sqrt{\frac{n}{\overline{n}}}\right) \sin\left(\frac{\pi}{2}\sqrt{\frac{n+1}{\overline{n}}}\right) \right. \\
&\qquad \left. -\tilde{c}_n^2 \cos\left(\frac{\pi}{2}\sqrt{\frac{n+1}{\overline{n}}}\right) \cos\left(\frac{\pi}{2}\sqrt{\frac{n}{\overline{n}}}\right) \right\}.
\end{aligned} \tag{7.2}$$

The real amplitudes $\{\tilde{c}_k\}$ of the optimal drive state can be computed in several ways. The exact coefficients are obtained as a solution of the eigenvalue equation (6.2), but they may as well be approximated with the squeezed cat states [Eq. (6.5)] or the normal distribution [Eq. (6.8)].

Evaluated with the optimal amplitudes, Eq. (7.2) presents the highest NOT gate fidelity that can be achieved with a single resonant pulse of a given average energy. It might be surprising that an upper bound exists at all. By the arguments presented in Sec. 6.1, squeezing the coherent state allows us to reduce the energy uncertainty at the cost of increasing entanglement and mixing. The upper bound utilizes the optimal balance between

these two.

7.1 Limit of infinite number of photons

We expect the upper bound to approach unity when $\overline{n} \to \infty$, since the coherent state is known to implement a perfect NOT gate in this limit. To this end, we expand $F_{\mathrm{b}}(\overline{n})$ in Eq. (7.2) in the first non-trivial order of $\overline{n}^{-1}$. Using Eq. (6.8) stemming from the normal distribution, we show in appendix B that the upper bound assumes the from

$$F_{\mathrm{b}}(\overline{n}) = 1 - \frac{4\mathrm{e}^{2s} + \mathrm{e}^{-2s}\pi^2}{16\overline{n}} + \mathcal{O}\left(\overline{n}^{-2}\right). \tag{7.3}$$

This expression allows us to solve for the optimal squeezing parameter s, completing our solution of the optimal states. Computing $\partial F_{\mathrm{b}}/\partial s = 0$ yields

$$-8\mathrm{e}^{2s} + 2\pi^2\mathrm{e}^{-2s} = 0 \quad \Rightarrow s = \frac{1}{2}\ln\frac{\pi}{2}. \tag{7.4}$$

With this value, the squeezed cat state yields the highest gate fidelity. To obtain Eq. (7.3), we assumed the limit $\overline{n} \to \infty$, but our numerical studies show that $s = \frac{1}{2}\ln\frac{\pi}{2}$ is the optimal value even for small $\overline{n}$.

Finally, the approximate upper bound is given by

$$F_{\mathrm{b}}(\overline{n}) = 1 - \frac{\pi}{4\overline{n}}. \tag{7.5}$$

The exact upper bound together with Eq. (7.5) are shown in Fig. 7.1. For the usual non-squeezed coherent drive state a similar calculation yields

$$F_{\min}^{\mathrm{coherent}}(\overline{n}) = 1 - \frac{4 + 4\pi + \pi^2}{16\overline{n}}. \tag{7.6}$$

This implies that the gate error $\mathcal{E}_{\max} \equiv 1 - F_{\min}$ for a coherent state is $\mathcal{E}_{\max}^{\mathrm{coherent}}(\overline{n}) \approx 2.1\,[1 - F_{\mathrm{b}}(\overline{n})]$, i.e., more than twice the optimal even in the limit $\overline{n} \to \infty$.

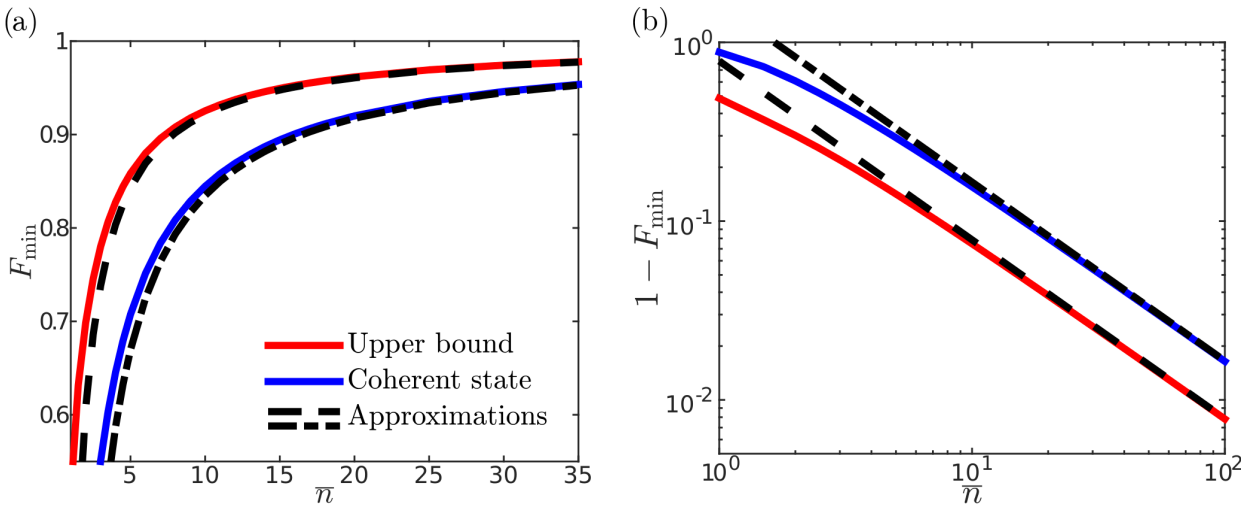

Figure 7.1: (a) NOT gate fidelities $F_{\min}$ as functions of the average photon number $\overline{n}$ of the initial drive state. The exact upper bound has been computed using the numerically solved optimal state. $F_{\min}$ of the coherent state and the first order approximations [Eqs. (7.5) and (7.6)] are shown for comparison. (b) Same as in (a), but maximum error $\mathcal{E}_{\max} = 1 - F_{\min}$ in a logarithmic scale.

8 Recycling the drive state

In the previous chapters, we studied the NOT gate fidelity for a single qubit driven by a single bosonic mode. After an interaction period with a qubit of unknown value, the drive and the qubit are entangled and have possibly exchanged energy. Thus the state of the drive is strictly speaking unknown and potentially useless for subsequent operations. However, the initialization of a new drive pulse for every gate would consume a great amount of energy in a large-scale quantum computer and it would be beneficial to use the same pulse for multiple operations. To make this recycling possible, the drive state must be purified and restored to its original state. Rather surprisingly, this can be achieved using ancilla qubits. The entanglement and excess energy of the field, originating from the quantum back-action in the previous gates, are transferred to the ancillae, rendering the drive itself pure. This treatment steers the drive to a stable state that can perform high-fidelity operations on the computational qubits.

Similar kind of steering has been investigated in at least two previous works. In Refs. [37, 38], it has been shown that a thermalized or a flat drive state can be driven into a pure, stable state by sequentially coupling qubits in specific states to it. Slosser [37] notes that with certain parameters, the resulting stable state resembles the coherent state. However, no previous work has studied the effect of coupling the drive to qubits in unknown states, nor how the purified drive state can be used in computational operations.

8.1 Extended system

Here, the system under consideration is a collection of qubits sequentially interacting with the same drive pulse. The qubits are divided into two categories: computational and ancilla qubits. This division is only conceptual, physically the qubits may be similar. As in the previous chapters, our goal is to implement the NOT gate on the computational qubits. On the other hand, the ancilla qubits are nothing but an information and energy dump and their initial values are chosen to optimize our protocol. The Jaynes–Cummings interaction takes place between a single qubit and the drive at a given instant of time. We assume that the state of the ancilla qubits can be accurately reset by external means when needed.

The recycling protocol is as follows: first, a drive state is prepared and used to rotate a new computational qubit. This is a standard π rotation on a qubit with an unknown value, during which the drive evolves into a slightly different state. Second, an auxiliary qubit with specifically chosen value interacts with the drive, after which the ancillary qubit is discarded or reset. If the value of the ancilla qubit is chosen properly, the drive will

evolve towards a stable state that can again implement a high-fidelity rotation. This step is repeated with multiple ancilla qubits until a desired accuracy for the refreshed drive state is reached. Subsequently we can implement another rotation on a new computational qubit without creating a new drive pulse.

To be precise, the density operator of the whole system should be written as the product of the two-level density operators of the qubits ($\hat{\chi}_i$) and that of the drive ($\hat{\sigma}$) as

$$\hat{\rho} = \hat{\chi}_0 \otimes \hat{\chi}_1 \otimes \hat{\chi}_2 \otimes ... \otimes \hat{\sigma}. \tag{8.1}$$

But since the drive only interacts sequentially with the qubits, we can describe the ith interaction by tracing over all qubit spaces not involved in it. The relevant density operator corresponding to the ith iteration is thus $\hat{\rho}_i = \hat{\chi}_i \otimes \hat{\sigma}_i$, where $\hat{\sigma}_i$ denotes the state of the drive at the beginning of the ith interaction. We assume that the qubit states are initially pure, but the evolving drive may not be. Using Eqs. (4.19) and (4.20), the ith iteration of the drive state is given by

$$\hat{\sigma}_i = \mathrm{Tr}_{\mathrm{Q}_{i-1}} \left[\hat{U}(t) \left(|\chi_{i-1}\rangle\langle\chi_{i-1}| \otimes \hat{\sigma}_{i-1} \right) \hat{U}^\dagger(t) \right], \tag{8.2}$$

where the temporal evolution operator $\hat{U}(t)$ is again given by Eq. (4.18).

8.2 Requirements for the protocol

8.2.1 Purity restoration

In order to our refresh protocol to work, we need to find ancilla qubits that both purify the drive state and steer it towards its initial state. In addition, we want to keep the interaction time the same throughout the protocol and hence the mean photon number should not change. The initial drive state should be chosen so that it is able to perform a precise rotation. We search for potential ancilla qubits by plotting the change in purity

$$\begin{aligned} \Delta P &= P(\hat{\sigma}_{i+1}) - P(\hat{\sigma}_i) = \mathrm{Tr}_{\mathrm{D}} \left(\hat{\sigma}_{i+1}^2 - \hat{\sigma}_i^2 \right) \\ &= \mathrm{Tr}_{\mathrm{D}} \left[\left\{ \mathrm{Tr}_{\mathrm{Q}_i} \left[\hat{U}(t) \left(|\chi_i\rangle\langle\chi_i| \otimes \hat{\sigma}_i \right) \hat{U}^\dagger(t) \right] \right\}^2 - \hat{\sigma}_i^2 \right] \end{aligned} \tag{8.3}$$

as a function of the ancilla qubit state $|\chi_i\rangle = \sqrt{1 - |z_\mathrm{a}|^2}\,|\mathrm{g}\rangle + z_\mathrm{a}\,|\mathrm{e}\rangle$. Starting from a pure drive state, we can only decrease its purity. Therefore we study a state that represents the drive during the protocol. Figure 8.1 shows the purity change for a drive state $\hat{\sigma}_{10}$

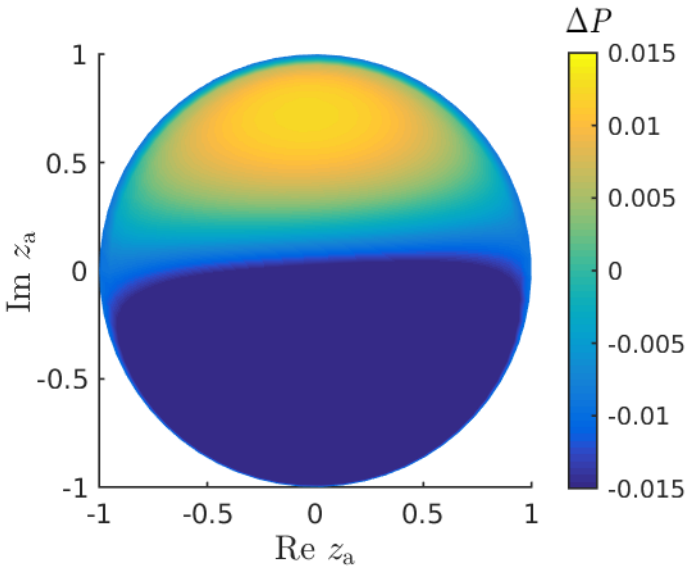

Figure 8.1: Purity change of a drive state due to the interaction with an ancilla qubit initialized in a state corresponding to z_a. The initial drive state $\hat{\sigma}_{10}$ was obtained by letting a coherent state with $\overline{n} = 25$ interact with 10 qubits in randomly chosen states. The interaction time corresponds to a π rotation. The plotted purity change is $\Delta P = P(\hat{\sigma}_{11}) - P(\hat{\sigma}_{10})$, where $\hat{\sigma}_{11}$ is the result of the evolution of $\hat{\sigma}_{10} \otimes |\chi(z_a)\rangle \langle\chi(z_a)|$.

that was initially in a coherent state $\hat{\sigma}_0 = |D_\alpha\rangle\langle D_\alpha|$ and has subsequently interacted with ten qubits in random pure states. The change ΔP is positive in a rather large region around $z_a = i/\sqrt{2}$, suggesting that the purity of the drive will increase with the next interaction. This feature persists across any number of interactions. Therefore we choose $z_a = i/\sqrt{2} \Leftrightarrow |\chi_i\rangle = (|g\rangle + i\,|e\rangle)/\sqrt{2}$ as our candidate for a purifying ancilla state. Even if this superposition state is not prepared precisely, the protocol should increase the purity since the purity-enhancing region in Fig. 8.1 is relatively large.

Similarly, if the initial state is $|D_{-\alpha}\rangle$, the purity increasing qubit value is around $z = -i/\sqrt{2}$. Other drive states do not increase the purity as much as the coherent one. For the optimal squeezed cat state $|\Sigma^{\pm}\rangle$ discovered in the previous chapter, the purity change is consistently negative for all values of z_a. Hence, $|\Sigma^{\pm}\rangle$ can not be used for the recycling protocol.

8.2.2 Energy restoration

In addition to increasing the purity, the ancilla state $|\chi_i\rangle = (|g\rangle + i\,|e\rangle)/\sqrt{2}$ has an interesting property of restoring the mean photon number of the drive. This can be studied by computing the change in the photon expectation value during one interaction. Computing

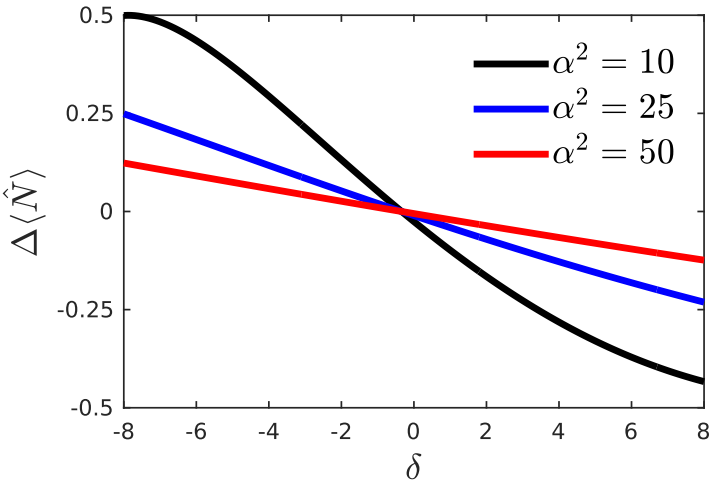

Figure 8.2: Change of the average photon number $\Delta\langle\hat{N}\rangle$ in an initial drive state $\left|\mathrm{D}_{\sqrt{\alpha^2+\delta}}\right\rangle$ as a function of the deviation δ. The change results from an interaction of the drive with an ancilla qubit prepared in the state $(|\mathrm{g}\rangle + i\,|\mathrm{e}\rangle)/\sqrt{2}$ for time $t = \pi/(2g\alpha)$.

$\langle\hat{N}\rangle_i = \mathrm{Tr}_\mathrm{D}(\hat{N}\hat{\sigma}_i)$ using Eq. (8.2) yields

$$\begin{aligned}\Delta\langle\hat{N}\rangle_i &= \langle\hat{N}\rangle_{i+1} - \langle\hat{N}\rangle_i = \mathrm{Tr}_\mathrm{D}\left(\hat{N}\hat{\sigma}_{i+1} - \hat{N}\hat{\sigma}_i\right) \\ &= \frac{1}{2}\sum_{k=0}^{\infty}\sigma_{k,k}\left[\sin^2\left(gt\sqrt{k+1}\right) - \sin^2\left(gt\sqrt{k}\right)\right] + \sin\left(2gt\sqrt{k+1}\right)\mathrm{Re}\,\sigma_{k,k+1}, \quad (8.4)\end{aligned}$$

where $\{\sigma_{k,l}\}$ are the matrix elements of the initial density operator $\hat{\sigma}_i$. Fixing the interaction time to $t = \pi/(2g\alpha)$, we show in Fig. 8.2 this difference for states $\left|\mathrm{D}_{\sqrt{\alpha^2+\delta}}\right\rangle$. The difference is accurately proportional to the offset, $\Delta\langle\hat{N}\rangle \propto -\delta$, for $\delta \ll \alpha^2$. Even for states that have interacted with numerous qubits and have suffered substantial decoherence, similar results are obtained.

The interaction with the ancilla qubit acts as negative feedback. The more the drive has gained excess photons from interactions with the computational qubits, the more likely it is to lose them for the ancillae. On the other hand, if the drive has lost photons, the interaction is likely to restore them. Increasing α decreases the slope in Fig. 8.2, implying that drive states with large amount of photons are more stable.

8.3 Refresh protocol

Above, we showed that the ancilla state $|\chi_i\rangle = (|\mathrm{g}\rangle + i\,|\mathrm{e}\rangle)/\sqrt{2}$ is able to both increase the purity and restore the photon number of the drive state. Finally, we test our protocol with

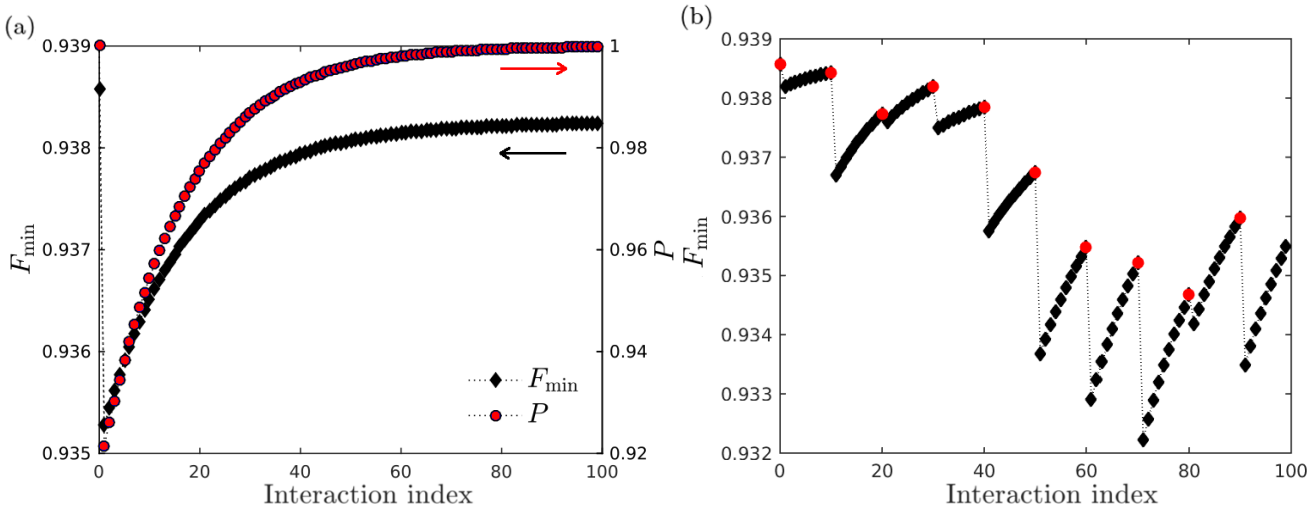

Figure 8.3: (a) Purity of the drive state (P, red dots, right axis) and the minimum fidelity ($F_{\min}$, black dots, left axis) of a hypothetical rotation as functions of the number of interaction periods between the drive state and the qubits. The initial drive state is a coherent state with $\overline{n} = 25$. The first interaction is with a computational qubit of a random value. The following 99 interactions are each with an individual correcting ancilla qubit prepared in the state $(|\mathrm{g}\rangle + i\,|\mathrm{e}\rangle)/\sqrt{2}$. (b) Same as (a), but with 9 corrections per iteration and only $F_{\min}$ shown. The red dots indicate interaction with computational qubits initialized to random pure states.

the following sequence:

1. **Preparation:** Prepare the drive state to $\hat{\sigma}_0 = |\mathrm{D}_\alpha\rangle\langle\mathrm{D}_\alpha|$ with a given α.
2. **Ancilla reset:** Initialize m ancilla qubits to the state $|\chi_i\rangle = (|\mathrm{g}\rangle + i\,|\mathrm{e}\rangle)/\sqrt{2}$.
3. **NOT gate:** Let the drive and a new computational qubit interact for a time period $t = \pi/(2g\alpha)$. The initial value of the qubit is chosen randomly.
4. **Refresh:** Let the drive and an ancilla qubit interact for a time $t = \pi/(2g\alpha)$. Repeat for each ancilla.
5. **Continue** from step 2.

Figure 8.3 demonstrates that the above routine works. The temporal evolution of each iteration is given by Eq. (8.2). After each interaction in steps 3 and 4, the purity of the drive state is evaluated with Eq. (2.19) and the minimum fidelity is given by

$$F_{\min} = \min_{\hat{\chi}} \mathrm{Tr}_{\mathrm{Q}} \left\{ \mathrm{Tr}_{\mathrm{D}} \left[\hat{U}(t) \left(\hat{\chi} \otimes \hat{\sigma}_i \right) \hat{U}^{\dagger}(t) \right] \hat{\sigma}_{\mathrm{x}} \hat{\chi} \hat{\sigma}_{\mathrm{x}} \right\}, \tag{8.5}$$

where $\hat{\sigma}_i$ is defined in Eq. (8.2).

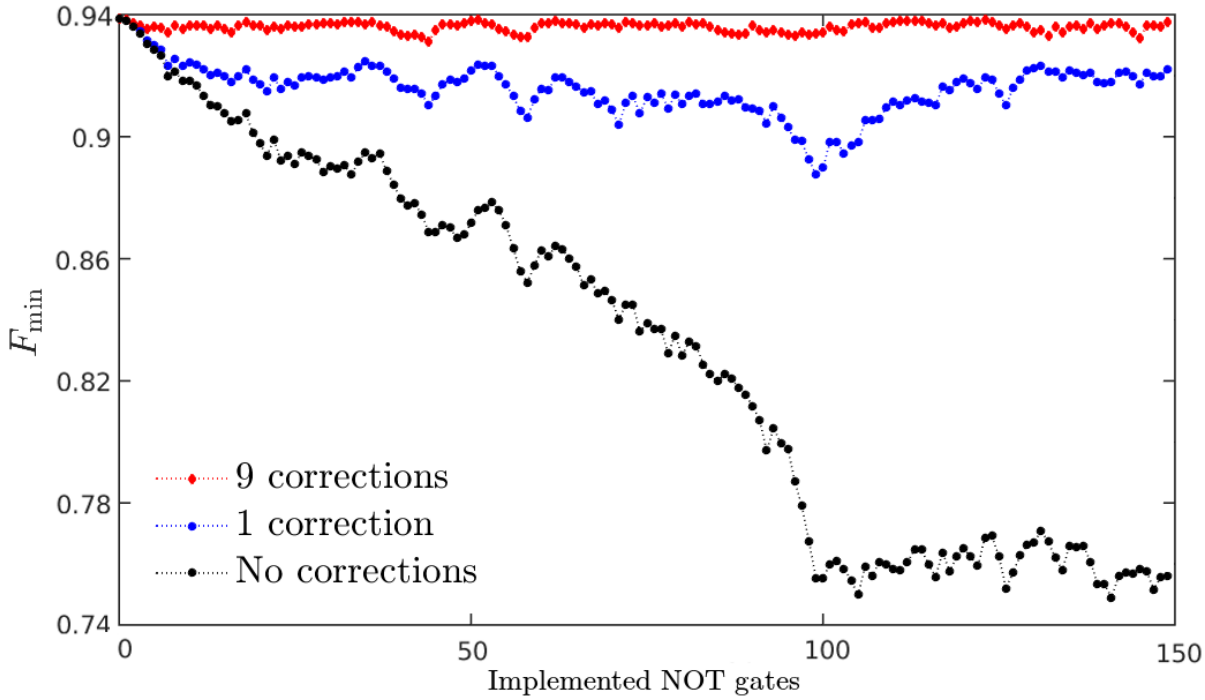

Figure 8.4: Gate fidelity as a function of the number of implemented NOT gates. A drive state is repeatedly applied to implement the NOT gate on different computational qubits with 0, 1, or 9 correcting ancilla qubits between the gates. The ancilla qubits are initialized to a state given in the main text. The random states of the computational qubits are identical for each number of corrections.

Clearly, the randomized computational qubits disturb the ability of the drive to perform a subsequent rotation but the perturbation is corrected by the ancilla qubits. With increasing number of corrections, the purity of the state indeed approaches unity after the initial disruption. The gate fidelity is also improved, but does not quite reach its initial value. The restoring effect is also visible in Fig. 8.3b: the further the state is thrown off from the equilibrium, the stronger the following corrections are. Apparently, no single deviation is large enough to break the drive state completely before it is refreshed.

Finally, the ratio of corrections per gate operation is studied in Fig. 8.4 using $\alpha = \sqrt{25}$. We observe that without any corrections, the gate fidelity decays rapidly but even a single correction per gate operation is enough to keep the fidelity mostly above 90%. With 9 corrections, the gate fidelity remains above 93%.

These results show that ancilla qubits can be used to refresh the drive, hence allowing it to implement high-fidelity NOT gates indefinitely. For the physical realization, there are two obstacles. The circuit architecture has to be designed such that the drive state is guided

to interact with the desired qubits sequentially. Another challenge is the preparation of the ancilla qubits in the superposition state. Preparing the ancilla qubits increases the complexity of the system and requires additional energy. Fortunately, the preparation need not be very precise. As Fig. 8.1 shows, it is enough that the ancilla qubit is relatively close to the optimal for the protocol to work.

9 Discussion

A large-scale quantum computer, capable of solving complex problems of practical interest, requires millions, if not hundreds of millions of physical qubits [18]. Controlling each qubit individually with high precision requires a lot of power to be dissipated at the operation temperature of the computer, and hence it is important to investigate all possibilities of mitigating the energy consumption in qubit control . In this thesis, we have studied two options: the optimization of the resonant drive state for minimal photon number needed to implement the X and Y rotation gates in the Jaynes–Cummings model, and the possibility of recycling the drive state using ancillary qubits to refresh the state.

In Ch. 5, we developed a method to solve the drive state that maximizes the gate fidelity of a given quantum operation and in Ch. 6, this method was applied to the NOT gate. The optimal state that maximizes the gate fidelity was found to be a superposition of slightly squeezed coherent states of opposite phase. These optimal drive states also define an upper bound for the maximum gate fidelity for a given mean number of photons in the pulse. The upper bound was found to approach unity inversely proportionally to the mean photon number. Similar results were obtained for the Pauli Y gate. The optimal states balance between two error sources: the uncertainty of the driving energy and the entanglement. The coherent state, typically used to model a classical state of light, was found to produce gate errors twice as large compared to the lower bound. The average state fidelities for the optimal and coherent drive states are nearly equal. Since the optimal drive states guarantee higher fidelity than the coherent states with the same average number of photons, they can also be used to achieve the same level of fidelity with fewer photons. This way, the optimal states may be used to reduce the energy needed for quantum computing.

Achieving and observing the upper bound should be possible with existing technology, since the coherent superposition of microwave pulses has been demonstrated in microwave cavity wave-guides [39, 27]. The practical question is whether it is worth the effort to use the optimal states. The answer depends on the experimental setup and on how accurately such states can be produced. If producing the squeezed superpositions requires a lot more energy or is prone to errors, the benefits of optimization may be too small. Nevertheless, an experimental demonstration of exceeding the coherent drive state in terms of gate fidelity would be of great fundamental value. Optionally, the coherent superposition could be replaced with a statistical mixture, which has an identical effect in the limit of many photons.

In the future, one may generalize the results of this thesis to the case of non-resonant, dispersive interaction. In the resonant case assumed in this thesis, the optimization method

of Ch. 5 only finds the optimal drive states for gates that rotate the qubit state about an axis lying in the xy-plane. Using the more general non-resonant system might allow optimization of other single-qubit gates, such as the Hadamard gate.

A different approach to energy-efficient quantum computing was considered in Ch. 8 where we investigated a refreshing protocol that allows a single drive state to implement multiple NOT operations. In our scheme, the drive pulse is guided to interact with qubits sequentially. Some of the qubits are computational qubits used in the actual quantum computing, while the rest are ancillary qubits designed to steer the drive towards its desired state. We found that if the ancilla qubits are prepared in a specifically chosen state, their interaction with the drive state has two restoring effects: the drive becomes more pure and hence less entangled with the previous qubits, and the mean photon number is driven towards a value set by the protocol. The latter feature is especially interesting since it does not depend on the history of the drive state. For example, if the drive has lost some amount of photons—to qubits or possibly even by dissipation—that amount can be added using the ancilla qubits. Furthermore, the desired drive state could be crafted even if the state is not initially a coherent state.

With enough corrective operations between the computational operations, the same drive state can be used indefinitely, maintaining its ability to perform high-fidelity gates. A drawback of this method is that the ancilla qubits themselves must be prepared in a superposition of the ground and excited states. Again, the loss of precision, energy, and computation time due to preparing the ancilla qubits should be smaller than the benefit achieved by the refreshing protocol. One option worth studying is a system of multiple refreshing pulses running in parallel, each pulse preparing the ancilla qubits needed for the adjacent pulse. While increasing the complexity of the system, this method might still cost less energy per computational flip than controlling each qubit individually.

A Finding the worst-case qubit for the NOT gate

In Sec. 6.1, we find the most optimal drive state for the NOT gate and for the qubit state that minimizes the fidelity, $F_{\min} = F(z_{\mathrm{w}})$. Here, we show that with certain reasonable restrictions, this worst-case qubit corresponds to $z_{\mathrm{w}} = \pm ir$ with $r \approx 1/\sqrt{2}$.

For $\hat{K} \mathrel{\widehat{=}} \begin{pmatrix} 0 & 1 \\ 1 & 0 \end{pmatrix}$, the fidelity function reads

$$F(z, \sigma_0, t) = \sum_k \left| \sum_{mn=0}^{1} \Gamma^k_{mn} c_{k+n-m} \right|^2 , \tag{A.1}$$

with the matrix Γ is given by

$$\Gamma^k = \begin{pmatrix} C^k z^* \sqrt{1-|z|^2} & -iS^k |z|^2 \\ -iS^{k+1}\left(1-|z|^2\right) & C^{k+1} z \sqrt{1-|z|^2} \end{pmatrix} . \tag{A.2}$$

First, we show that for this gate, the complex number z_{w} lies on the imaginary axis. Using Eqs. (A.1) and (A.2) and writing $z = r\mathrm{e}^{i\varphi}$, we observe that $F \propto |\Gamma_{nm}|^2$ has only terms proportional to $\mathrm{e}^{\pm 2i\varphi}$, $\mathrm{e}^{\pm i\varphi}$, and constant terms. In its domain $\varphi \in [0, 2\pi]$, $\mathrm{e}^{\pm 2i\varphi}$ has 2 cycles and $\mathrm{e}^{\pm i\varphi}$ has one. Thus, for a fixed r, F has a maximum of 2 sine-like periods and can have at most 4 critical points. Since φ is periodic, there are no more than 2 minima.

With certain assumptions, the locations of these minima are fixed to $\pm ir$. The derivative of F is given by

$$\begin{aligned} \partial_\varphi F &= \sum_k \left\{ c_k^* \sqrt{1-r^2} \left(izC^k - iz^* C^{k+1} \right) \right\} \sum_{nm} \Gamma^k_{mn} c_{k+m-n} + \text{c.c.} \\ &= 2\sqrt{1-r^2} \sum_k \mathrm{Im} \left\{ \sum_{nm} c_{k+m-n} c_k^* \Gamma^k_{mn} \left(z^* C^{k+1} - zC^k \right) \right\} . \end{aligned}$$

At points $z = \pm ir$, the matrix Γ becomes purely imaginary and we can separate the matrix elements from $\{c_j\}$. Evaluating the derivative yields

$$\begin{aligned} \partial_\varphi F|_{z=\pm ir} &= 2r\sqrt{1-r^2} \sum_k \mathrm{Im} \left\{ \sum_{nm} c_{k+m-n} c_k^* \Gamma^k_{mn} \left(\mp iC^{k+1} \mp iC^k \right) \right\} \\ &= \mp 2r\sqrt{1-r^2} \sum_k \left(C^{k+1} + C^k \right) \left(i\Gamma^k_{10} \mathrm{Im}\left\{ c_{k+1} c_k^* \right\} + i\Gamma^k_{01} \mathrm{Im}\left\{ c_{k-1} c_k^* \right\} \right) \end{aligned}$$

$$= \mp 2r\sqrt{1-r^2}\sum_k \left\{\left(C^{k+1}+C^k\right)\left(1-r^2\right)S^k - \left(C^{k+2}+C^{k+1}\right)r^2 S^{k+1}\right\}\mathrm{Im}\left\{c_{k+1}c_k^*\right\}.$$

This is zero for all r if $\mathrm{Im}\{c_{k+1}c_k^*\} = 0$. That is, the points $z = \pm ir$ are always critical points if $\{c_j\}$ are real, even, or odd. To make progress, we continue with the assumption that $\{c_j\}$ are real. To confirm that $z = \pm ir$ are indeed the two minima, we must show that $\partial_\varphi^2 F > 0$. The second derivative is given by

$$\begin{aligned}\partial_\varphi^2 F\big|_{z=\pm ir} &= 8\left(r^2-r^4\right)\sum_k C^k C^{k+1}|c_k|^2 \\ &\quad \mp 2r\left(1-r^2\right)^{3/2}\sum_k c_{k+1}c_k\left[S^k(C^k - C^{k+1}) + S^{k+1}(C^{k+1}-C^{k+2})\right] \quad \text{(A.3)}\end{aligned}$$

Let us study the behavior of the factor $C^kC^{k+1} = \cos\left(gt\sqrt{k}\right)\cos\left(gt\sqrt{k+1}\right)$ in the first term. The zeros of this expression come in pairs $\{k_n^+, k_n^-\}$ such that

$$k_n^+ = \frac{\pi^2(1+2n)^2}{4(gt)^2}, \quad k_n^- = k_n^+ - 1, \quad n \in \mathbb{N}.$$

Each pair is separated by unity, but the separation of subsequent pairs increases, $k_n^+ - k_{n-1}^+ \propto n$. Since C^kC^{k+1} is positive in the regions $]k_n^+, k_{n+1}^-[$ and negative in the regions $]k_n^-, k_n^+[$, we can conclude that C^kC^{k+1} is positive for most k. This holds at least for $gt \leq \pi/2$.

Equation (A.3) is of the form $a \mp b$, and by the above consideration it can be concluded that $a > 0$. If $z = \pm ir$ were both maximum points, we would obtain $\partial_\varphi^2 F(\pm ir) = a \mp b < 0 \Rightarrow 2a < 0$, i.e., a contradiction. Therefore at least one of the points $\pm ir$ is a minimum point.

In summary, we found that there are no more than 2 minima, and at least $z = ir$ or $z = -ir$ is a minimum. Thus z_w lie on the imaginary axis, provided that $\{c_j\}$ are real. Additionally, we need to show that the minimum is at $r = 1/\sqrt{2}$. Unfortunately, the derivative $\partial F(\pm ir)/\partial r$ is not independent of the $\{c_j\}$ amplitudes. It is approximately

$$\partial F(\pm ir)/\partial r \approx 4\sum_k \left[r^3\left(S^k c_{k-1}\right)^2 + \left(r^3-r\right)\left(S^{k+1}c_{k+1}\right)^2 - \left(2r^3-r\right)S^kS^{k+1}c_{k+1}c_{k-1}\right],$$

where we have neglected terms proportional to $\cos\left(gt\sqrt{k+1}\right) - \cos\left(gt\sqrt{k}\right)$ because their contribution is small compared to that of the other terms. Solving for the zero of this

expression yields

$$r = \sqrt{\frac{1}{1+h}}, \text{ where } \quad h = \frac{\sum c_k^2 \left(S^{k+1}\right)^2 - c_{k-1}c_{k+1}S^k S^{k+1}}{\sum c_k^2 \left(S^k\right)^2 - c_{k-1}c_{k+1}S^k S^{k+1}}.$$

Thus $h \approx 1$ for typical sets of $\{c_k\}$. We conclude that the worst-case qubit value is $z_{\mathrm{w}} \approx \pm i/\sqrt{2}$, assuming the coefficients c_j are real and that $t \leq \pi/2g$.

B Approximate upper bound of the gate fidelity

In Sec. 7.1, we compute the upper bound of the minimum fidelity for the NOT gate. This is carried out by inserting the approximate optimal drive coefficients [from Eq. (6.8)],

$$\tilde{c}_n(\alpha) = \sqrt{2}\left(2\pi \mathrm{e}^{-2s}\right)^{-1/4} \alpha^{-1/2} \exp\left[-\frac{\mathrm{e}^{2s}}{4}\left(\frac{n}{\alpha} - \alpha\right)^2\right] \cos^2(\pi n/2), \tag{B.1}$$

into

$$\begin{aligned} F_{\mathrm{b}}(\overline{n}) \;=\; & \frac{1}{2} + \frac{1}{2}\sum_{n=0}^{\infty}\left\{\tilde{c}_{n+1}\tilde{c}_{n-1}\sin\left(\frac{\pi}{2}\sqrt{\frac{n}{\overline{n}}}\right)\sin\left(\frac{\pi}{2}\sqrt{\frac{n+1}{\overline{n}}}\right)\right. \\ & \left. -\tilde{c}_n^2\cos\left(\frac{\pi}{2}\sqrt{\frac{n+1}{\overline{n}}}\right)\cos\left(\frac{\pi}{2}\sqrt{\frac{n}{\overline{n}}}\right)\right\}. \end{aligned} \tag{B.2}$$

Here, we outline how this expression can be approximated to the first order in $\overline{n}^{\,-1}$ in the limit $\overline{n} \to \infty$. Denoting the vanishing quantity by $\epsilon = \alpha^{-1} = \sqrt{\overline{n}}^{\,-1}$, Eq. (B.2) assumes the form

$$F_{\mathrm{b}}(\epsilon) \;=\; \frac{1}{2} + \frac{1}{2}\sum_{n}\left\{\tilde{c}_{n+1}\tilde{c}_{n-1}\sin\left(\frac{\pi}{2}\sqrt{n}\epsilon\right)\sin\left(\frac{\pi}{2}\sqrt{n+1}\epsilon\right) - \tilde{c}_n^2\cos\left(\frac{\pi}{2}\sqrt{n+1}\epsilon\right)\cos\left(\frac{\pi}{2}\sqrt{n}\epsilon\right)\right\}.$$

Inserting here the coefficients from Eq. (B.1) leads to

$$F_{\mathrm{b}}(\epsilon) = \frac{1}{2} + \frac{\epsilon \mathrm{e}^{s}}{\sqrt{2\pi}}\left(I_1 + I_2\right), \tag{B.3}$$

where I_1 and I_2 are given by

$$\begin{aligned} I_1 \;=\; & \sum_n \exp\left\{-\frac{\mathrm{e}^{2s}}{4}\left[(n+1)\epsilon - \epsilon^{-1}\right]^2\right\}\exp\left\{-\frac{\mathrm{e}^{2s}}{4}\left[(n-1)\epsilon - \epsilon^{-1}\right]^2\right\} \\ & \times \cos^4\left[\frac{\pi}{2}(n+1)\right]\sin\left(\frac{\pi}{2}\sqrt{n}\epsilon\right)\sin\left(\frac{\pi}{2}\sqrt{n+1}\epsilon\right) \end{aligned}$$

and

$$I_2 = -\sum_n \exp\left[-\frac{\mathrm{e}^{2s}}{2}\left(n\epsilon-\epsilon^{-1}\right)^2\right]\cos^4(\pi n/2)\cos\left(\frac{\pi}{2}\sqrt{n+1}\epsilon\right)\cos\left(\frac{\pi}{2}\sqrt{n}\epsilon\right).$$

The $\cos^4$ factors in I_1 and I_2 cause the summations to have only odd and even terms, respectively. Hence we can change the summation variables such that

$$I_1 = \sum_{m=0}^{\infty}\exp\left(-\frac{\mathrm{e}^{2s}}{4}\left\{\left[(2m+2)\epsilon-\epsilon^{-1}\right]^2+(2m\epsilon-\epsilon^{-1})^2\right\}\right)\sin\left(\frac{\pi}{2}\sqrt{2m+1}\epsilon\right)\sin\left(\frac{\pi}{2}\sqrt{2m+2}\epsilon\right)$$

and

$$I_2 = -\sum_{m=0}^{\infty}\exp\left[-\frac{\mathrm{e}^{2s}}{2}\left(2m\epsilon-\epsilon^{-1}\right)^2\right]\cos\left(\frac{\pi}{2}\sqrt{2m+1}\epsilon\right)\cos\left(\frac{\pi}{2}\sqrt{2m}\epsilon\right).$$

These expressions cannot be expanded in Taylor series around the point $\epsilon = 0$ because the exponential factors contain divergent arguments of ϵ^{-1}. This is solved by changing the variables to

$$x = 2m\epsilon-\epsilon^{-1} \Leftrightarrow m = \frac{x+\epsilon^{-1}}{2\epsilon}.$$

Furthermore, we change the summation into an integral. This is justified in the limit $\overline{n}\to\infty$, where the functions are rather smooth and have support on a region much wider than unity. The summations are replaced by $\sum_m \to \int \mathrm{d}m \to \int \mathrm{d}x/(2\epsilon)$ and the bounds by $[0,\infty]\to[-\epsilon^{-1},\infty]\to[-\infty,\infty]$. The integrals

$$I_1 = \exp\left(-\mathrm{e}^{2s}\epsilon^2\right)\int_{-\infty}^{\infty}\exp\left[-\mathrm{e}^{2s}\left(\frac{1}{2}x^2+\epsilon x\right)\right]\sin\left(\frac{\pi}{2}\sqrt{x\epsilon+1+\epsilon^2}\right)\sin\left(\frac{\pi}{2}\sqrt{x\epsilon+1+2\epsilon^2}\right)\frac{\mathrm{d}x}{2\epsilon}$$

and

$$I_2 = -\int_{-\infty}^{\infty}\exp\left(-\frac{\mathrm{e}^{2s}}{2}x^2\right)\cos\left(\frac{\pi}{2}\sqrt{x\epsilon+1+\epsilon^2}\right)\cos\left(\frac{\pi}{2}\sqrt{x\epsilon+1}\right)\frac{\mathrm{d}x}{2\epsilon}$$

can be computed by expanding the integrands about $\epsilon = 0$ and applying textbook formulas for the resulting Gaussian integrals. Thus we obtain

$$I_1 = \sqrt{2\pi}\mathrm{e}^{-s}\left(\frac{1}{2\epsilon}-\frac{8+\mathrm{e}^{-4s}\pi^2}{32\mathrm{e}^{-2s}}\mathrm{e}^{2s}\epsilon\right)+\mathcal{O}(\epsilon^3)$$

and

$$I_2 = -\sqrt{2\pi}\mathrm{e}^{-s}\frac{\mathrm{e}^{-2s}\pi^2}{32}\epsilon+\mathcal{O}(\epsilon^3).$$

Inserting these into Eq. (B.3) results in

$$\begin{aligned} F_{\mathrm{b}} &= \frac{1}{2} + \frac{\epsilon \mathrm{e}^{s}}{\sqrt{2\pi}} \left(I_1 + I_2\right) = 1 - \frac{4\mathrm{e}^{2s} + \mathrm{e}^{-2s}\pi^2}{16}\epsilon^2 + \mathcal{O}(\epsilon^4) \\ &= 1 - \frac{4\mathrm{e}^{2s} + \mathrm{e}^{-2s}\pi^2}{16\overline{n}} + \mathcal{O}(\overline{n}^{\,-2}), \end{aligned} \tag{B.4}$$

which is the upper bound for the NOT gate fidelity given in the main text.

References

[1] M. Nielsen and I. Chuang, *Quantum Computation and Quantum Information*, Cambridge University Press, Cambridge, 2000.

[2] T. C. Ladd *et al.*, *Quantum computers*, Nature **464**, 45 (2010).

[3] D. Deutsch and R. Jozsa, *Rapid Solution of Problems by Quantum Computation*, Proc. R. Soc. Lond. A **439**, 553 (1992).

[4] P. Shor, *Algorithms for quantum computation: discrete logarithms and factoring*, in *Foundations of Computer Science, 1994 Proceedings., 35th Annual Symposium on*, pages 124–134, 1994.

[5] L. K. Grover, *Quantum mechanics helps in searching for a needle in a haystack*, Phys. Rev. Lett. **79**, 325 (1997).

[6] D. DiVincenzo, *The physical implementation of quantum computation*, Fortschr. Phys. **48**, 771 (2000).

[7] P. Domokos, *Simple cavity-QED two-bit universal quantum logic gate: The principle and expected performances*, Phys. Rev. A **52**, 3554 (1995).

[8] R. Blatt and D. Wineland, *Entangled states of trapped atomic ions*, Nature **453**, 1008 (2008).

[9] E. Knill, R. Laflamme, and G. J. Milburn, *A scheme for efficient quantum computation with linear optics*, Nature **409**, 46 (2001).

[10] C. Negrevergne *et al.*, *Benchmarking Quantum Control Methods on a 12-Qubit System*, Phys. Rev. Lett. **96**, 170501 (2006).

[11] M. Veldhorst *et al.*, *An addressable quantum dot qubit with fault-tolerant control-fidelity*, Nat. Nano **9**, 981 (2014).

[12] J. Kelly *et al.*, *State preservation by repetitive error detection in a superconducting quantum circuit*, Nature **519**, 66 (2015).

[13] J. Clarke and F. K. Wilhelm, *Superconducting quantum bits*, Nature **453**, 1031 (2008).

[14] B. W. Shore and P. L. Knight, *The Jaynes-Cummings Model*, J. Mod. Opt. **40**, 1195 (1993).

[15] R. Barends *et al.*, *Superconducting quantum circuits at the surface code threshold for fault tolerance*, Nature **508**, 500 (2014).

[16] M. Veldhorst *et al.*, *A two-qubit logic gate in silicon*, Nature **526**, 410 (2015).

[17] J. Preskill, *Reliable quantum computers*, Proc. R. Soc. Lond. A **454**, 385 (1998).

[18] A. G. Fowler *et al.*, *Surface codes: Towards practical large-scale quantum computation*, Phys. Rev. A **86**, 032324 (2012).

[19] B. M. Terhal, *Quantum error correction for quantum memories*, Rev. Mod. Phys. **87**, 307 (2015).

[20] V. V. Dodonov, *'Nonclassical' states in quantum optics: a 'squeezed' review of the first 75 years*, J. Opt. B **4**, R1 (2002).

[21] C. M. A. Dantas, N. G. d. de Almeida, and B. Baseia, *Statistical properties of the squeezed displaced number states*, Braz. J. Phys. **28**, 00 (1998).

[22] R. Henry and S. Glotzer, *A squeezed-state primer*, Am. J. Phys. **56**, 318 (1988).

[23] J. Sakurai, *Modern quantum mechanics*, Addison-Wesley, Boston, 1994.

[24] N. A. Peters, T.-C. Wei, and P. G. Kwiat, *Mixed-state sensitivity of several quantum-information benchmarks*, Phys. Rev. A **70**, 052309 (2004).

[25] M. Möttönen *et al.*, *High-fidelity one-qubit operations under random telegraph noise*, Phys. Rev. A **73**, 022332 (2006).

[26] H.-P. Breuer and F. Petruccione, *The theory of open quantum systems*, Oxford University Press, Oxford, 2002.

[27] B. Vlastakis *et al.*, *Deterministically Encoding Quantum Information Using 100-Photon Schrödinger Cat States*, Science **342**, 607 (2013).

[28] E. Jaynes and F. Cummings, *Comparison of quantum and semiclassical radiation theories with application to the beam maser*, Proc. IEEE **51**, 89 (1963).

[29] J. Martinis and K. Osborne, *Superconducting qubits and the physics of Josephson junctions*, arXiv:cond-mat/0402415 (2004).

[30] J. Koch *et al.*, *Charge-insensitive qubit design derived from the Cooper pair box*, Phys. Rev. A **76**, 042319 (2007).

[31] P. Jones, J. Salmilehto, and M. Möttönen, *Highly Controllable Qubit–Bath Coupling Based on a Sequence of Resonators*, J. Low Temp. Phys. **173**, 152 (2013).

[32] C. Gerry and P. Knight, *Introductory quantum optics*, Cambridge University Press, Cambridge, 2005.

[33] V. Bužek *et al.*, *Schrödinger-cat states in the resonant Jaynes-Cummings model: Collapse and revival of oscillations of the photon-number distribution*, Phys. Rev. A **45**, 8190 (1992).

[34] J. Larson, *Dynamics of the Jaynes-Cummings and Rabi models: old wine in new bottles*, Physica Scr. **76**, 146 (2007).

[35] J. Johansson *et al.*, *Vacuum Rabi Oscillations in a Macroscopic Superconducting Qubit LC Oscillator System*, Phys. Rev. Lett. **96**, 127006 (2006).

[36] J. Gea-Banacloche, *Atom- and field-state evolution in the Jaynes-Cummings model for large initial fields*, Phys. Rev. A **44**, 5913 (1991).

[37] J. J. Slosser, P. Meystre, and S. L. Braunstein, *Harmonic oscillator driven by a quantum current*, Phys. Rev. Lett. **63**, 934 (1989).

[38] J. Åberg, *Catalytic Coherence*, Phys. Rev. Lett. **113**, 150402 (2014).

[39] G. Kirchmair *et al.*, *Observation of quantum state collapse and revival due to the single-photon Kerr effect*, Nature **495**, 205 (2013).